DEVELOPMENT OF A HYBRID FINITE ELEMENT METHOD FOR SOLVING INVERSE ENGINEERING PROBLEMS

by

XIYUN WANG

A dissertation submitted in partial fulfillment of the
requirements for the degree of

DOCTOR OF PHILOSOPHY IN MECHANICAL ENGINEERING

2024

Oakland University
Rochester, Michigan

Doctoral Advisory Committee:

Randy J. Gu, Ph.D., Chair
Lianxiang Yang, Ph.D.
Tamas Horvath, Ph.D.
Yin-Ping Chang, Ph.D.

I want to thank my parents for their support. Thanks to my wife for her companionship over the years. Thanks to my advisor for his instruction and teaching. Thank you all, without you, I could not have achieved what I have today.

ACKNOWLEDGMENTS

First and foremost, I would like to express my deepest gratitude to my advisor, Professor Randy J. Gu, for his meticulous guidance in my academic pursuits, his trust in me, and the encouragement that has brought me to where I am today. I also want to thank Professor Yin-ping Chang for supporting and affirming my work as a Teaching Assistant. Additionally, I appreciate the guidance of the advisory committee over the years.

Xiyun Wang

ABSTRACT

DEVELOPMENT OF A HYBRID FINITE ELEMENT METHOD FOR SOLVING INVERSE ENGINEERING PROBLEMS

by

XIYUN WANG

Adviser: Randy J. Gu, Ph.D.

The ill-posed boundary value problems, such as contact problems, adhesive joint analysis, and damage identification, are of foremost importance in the design and manufacturing of machines. The analysis of these problems has attracted considerable attention from engineers and researchers in various industries. This dissertation presents a novel hybrid finite element method for solving ill-posed boundary value problems through inverse engineering, with a focus on accurately determining contact stress, identifying damage, and analyzing adhesive joints in mechanical engineering. A significant aspect of this method involves integrating empirical measurements with numerical simulations to enhance both the accuracy and reliability of finite element analyses under insufficient boundary conditions. A constrained optimization framework is also employed in this study. The method is evaluated through seven case studies, which include assessments of plate bending, rigid contact problems, Hertzian contact problems, damage identification tasks, single lap joint, and T-peel joint evaluations. A novel constraint equation based on the gradient of the loading function is introduced as well. These case studies highlight the method's comprehensive applicability and effectiveness

across a range of complex engineering challenges. The dissertation outlines future work that aims to expand the method's application to three-dimensional problems, improve the optimization algorithms, and explore further applications. This work lays a foundation for advancing more complex and reliable modeling techniques in mechanical engineering, with significant implications for both research and industrial applications.

TABLE OF CONTENTS

TABLE OF CONTENTS

TABLE OF CONTENTS

LIST OF TABLES

LIST OF FIGURES

LIST OF FIGURES

LIST OF FIGURES

CHAPTER ONE

INTRODUCTION

The current study proposes the novel hybrid technique to determine the insufficient boundary from theoretical derivation incorporating experimental measurements. The ill-posed boundary value problems include frictionless contact problems, adhesive joint problems, and damage identification problems. In the first phase, a finite element system for the contact problem of the elastic objects is established. Experimental measurements, such as displacements on the free surface, are imposed on the finite element system as an additional constraint. The minimization scheme of the approach together with the solution algorithm are depicted in Chapter 3. In this study, the optimization program is launched by commercial code ANSYS [1], which includes direct optimization function with several different optimization method. The three widely used method are:

- Screening, it uses a simple approach based on sampling and sorting. It supports multiple objectives as well as all type of input parameters. It is usually used for global behavior study.
- NLPQL (Nonlinear Programming by Quadratic Lagrangian), the method is a gradient-base algorithm to provide a local optimization result.
- MOGA (Multi-Objective Genetic Algorithm), the method supports multiple objectives and aims at finding global optimum.

The detailed theory for NLPQL and GA are presented in Appendix A. Several examples are utilized to demonstrate the accuracy as well as efficiency of the proposed technique.

The major subject of this study is contact problems. The first numerical example given in Chapter 4 inspects a plate bending problem. It is a simple problem to demonstrate the new method. Another numerical example given in Chapter 5 inspects the contact between one rectangular block pressing against an elastic plane. In Chapter 6 the contact pressure between a washer and a bolt commonly found in the joining methods in automotive industry is tested using the proposed numerical technique. Chapter 7 proposed a cylinder lies on a block, which is a well-known Hertzian contact problem. The hertzian contact pressure is determined by the new technique. After a couple examples about the contact problem, the shear stress distribution along a single lap joint is checked. In Chapter 9 damage on a cantilever beam is characterized. The damage size and the damage location are identified by the proposed technique. Chapter 10 studies the application of the proposed method in T-peel joint and introduces a completely new set of constraint equations. Finally, the prospect of the hybrid numerical-empirical technique as well as its potential improvement and the future works are summarized in Chapter 11 - Conclusion.

CHAPTER TWO

LITERATURE REVIEW

2.1 Contact Problem

Contact mechanics deals with phenomena of critical importance for numerous physical, technical, and medical applications. In mechanical engineering along the scope of applications is immense, abundant examples cover ball bearings, gear drives, friction clutches, brakes, etc. The works of Hertz [2] and Boussinesq [3] are generally considered the beginning of classical contact mechanics. The solutions for the pressure distribution under a cylindrical punch and a sphere featured in those works certainly enjoy a high level of prominence [4]. Finite element method (FEM) and finite element analysis (FEA) are wildly used to solve contact problems. Most of the studies are theoretical base in that numerical calculations are done on purely theoretical formulation. For general kind of contact problems, the two widely used procedures to solve them are Lagrange's multiplier method and the penalty function method [5]. Both these methods operate on the variational or weighted residual formulation of the problem under consideration. Gu et al. [6] developed a modified penalty method replacing the constant penalty number with a penalty variable. The method is employed to solve problems involving objects with inadequate support at the start of the analysis which could not otherwise be solved using traditional penalty method or by many commercial finite element codes. In the past four decades, variety aspects related to contact problems solved by finite element method met a lot of success [7-14]. On the other front, research in experimental investigation to determine the contact stress between two objects has been ongoing for decades. Maniatty et al. [15] presented a study in that the boundary tractions and displacements in an elastically deformed two-dimensional (2D) body are calculated using experimentally determined or specified displacements or strains at a finite number of internal points.

2.2 Single Lap Joint

Many inventions and products are needed the assembling of numerous parts, frequently made of different materials. Joining materials together is a vital technique in the development of technology. Joining techniques have evolved over time to become more sophisticated, utilizing a variety of mechanical fasteners, various welding methods, and the use of adhesives, sealants, mortars, cements, and other binders to hold components together. Single lap joint is a typical classification of adhesive joints, which is one of the most commonly occurring joints and is the configuration most often used for testing adhesives [16].

Silva et al. [17] presented a comprehensive literature survey based on analytical models of adhesively bonded joints. Volkersen in 1938 proposed a shear lag model for analyzing shear stresses within adhesive joint [18]. The shear lag model has found broad applicability in the later studies. Ojalvo and Eidinoff [19] extended Volkersen's by examining the impact of adhesive thickness on the stress distribution using a more thorough shear strain/displacement equation for the adhesive layer. DeVries et al. [20] proposed the adhesive fracture of lap joints in terms of both the maximum stress criterion and the energy balance. The study shows an apparent difference in the adhesive fracture energy associated with crack growth for the different loading modes. The natural frequencies and loss factors of coupled longitudinal and flexural vibrations of adhesive joints have been studied by Saito and Tani [21]. This system consists of two parallel, identical elastic cantilevers that are lap-jointed over a distance from their free ends by a viscoelastic substance. In order to simplify calculations and improve research efficiency, two-dimensional models are widely used in the analysis of the lap joints. Sawa et al. [22] performed many investigations on the analysis of stresses and deformations in single-lap adhesive joints of similar adherends subjected to tensile loads. In the numerical calculations, the effects of Young's modulus ratio between the dissimilar adherends, the adherend thickness, the adherend lengths, and the adhesive thickness on the interface stress distributions were clarified. Zhao et al. [23] presented a two-dimensional (2D) analytical method that can provide an explicit closed-form solution for the prediction of elastic stresses in balanced single-lap adhesive-bonded joints. To derive a closed-form solution for the stress distribution in an adhesive single-lap joint, various simplified assumptions concerning the behavior of the adhesive and adherends have been made in many existing models. An explicit formulation is usually difficult to obtain in such sandwich structure due to several intrinsic factors, which should be considered simultaneously in the derivation of the governing equations to determine the adhesive stress distribution and joint strength. These factors are the adherend shear-lag effect, bending effect induced by the non-axial loading, end effects caused by the free surfaces at the ends of the adhesive layer, large rotations of the overlap adherends resulting from the eccentricity of loading path, nonlinear adhesive properties, and satisfaction of all natural/essential boundary conditions. The study of lap joints has evolved and become more refined during the last few decades [24-30]. Finite element analysis techniques were crucial during this time. He [31] reviewed the research and progress in FEA of adhesively bonded joints and presented the current trends in the application of FEA. It is argued that the FEA of adhesively bonded joints will facilitate future applications of adhesive bonding by allowing alternative parameters to be specified. This would enable many tests that would currently take too long or be too expensive to undertake in practice to be simulated.

2.3 Inverse Method

The study of inverse problems started in the early 20th century and has been widely investigated in various fields such as in medical research, bioengineering, astronomy, machine learning, material mechanics, optics, etc. Douglas [32] provided necessary and sufficient conditions for the solution to the inverse problem of Lagrangian mechanics to exist. In the current research, most of higher dimension cases are solved in the sense of Douglas. Finding the solution of an inverse problem requires sophisticated optimization algorithms. When the model is described by a large number of parameters, solving the linear system associated with the normal equations can be cumbersome. An algorithm for solving the forward problem can be summarized as dealing with numerical methods for the solution of linear systems and for the minimization of quadratic functions. The optimization methods are widely introduced in texts [33, 34]. Vito et al. [35] analyzed the relationship between the theory of statistical learning and the theory of ill-posed problems. The results shows that the consistency of algorithm can be traced back to convergence property of the Tikhonov regularization. An elegant concentration in equality in Hilbert spaces provides the probabilistic estimate of the noise. Martins [36] performed a comparative study on four identification strategies based on full-field measurements namely the finite element model updating, the constitutive equation gap method, the equilibrium gap method and the virtual fields method. Cooreman et al. [37]

proposed the method about identification of mechanical material behavior through inverse modeling and digital image correlation. The method allows the determination of averaged material parameters, based on the high information contents of heterogeneous strain fields. Kang et al. [38] presented an inverse optimization method for solving mechanical parameter identification problem of interfaces in actual multiphase composite materials. Joseph et al. [39], presented a method for the design of a structure with specified natural frequencies, which is based on the solution of a partial inverse eigenvalue problem. Following Joseph's research, Olsson et al. [40] used elements of a constraint matrix as design variables to formulate an inverse structural modification problem. To identify the dynamic loads, Sun et al. [41] proposed a novel improved regularization method with new regularization filter function that can resolve the ill-posed inverse problem existed in a Fredholm integral equation of the first kind. Wang et al. [42] investigated a time-domain method to estimate the unknown time histories of the external load. The dynamic loads were identified in the presence of unknown but bounded measurement errors. Song and Gu [43] presented an inverse algorithm to solve the contact forces and deformation using the finite element method which incorporated some measured displacements on the boundary with known surface traction. Svec [44] developed a finite element iterative procedure for determination of the contact region between the plate and the elastic half space. Lin et al. [45] proposed an experimental characterization of frictional line contact by digital image correlation and inverse method. The method can provide reliable identification results. However, in Lin's study, the inverse program employed a strong constraint, that the contact pressure was assumed as in Hertzian distribution, leads to the severe limitation of the method.

2.4 Damage Identification

Damage identification analysis is a special classification as inverse problem in computational mechanics and structural engineering. Most of damage identification methods is based on the vibration characteristic, which is also known as Structural Health Monitoring (SHM). The studies about the damage identification method before 21st century were reviewed comprehensively by Doebling [46]. Fan and Qiao [47] presented a review on modal parameter-based damage identification methods for beam- or plate-type structures. They argued that the damage identification techniques can be classified into four main categories according on the vibration features: Natural frequency-based techniques, curvature-based techniques, mode shape-based techniques, and techniques that combine mode shapes and frequencies. Kim [48] proposed an improved damage identification method based on modal information. A new non-destructive damage detection algorithm and two existing methods are evaluated by predicting damage locations and estimating severities of damage in a two-span continuous beam. Due to requirements like comprehensive measured data and modal information needed before and after damaged states, classic damage detection methods are constrained in their practical applicability. Strain damage indices have received a lot of interest because of how sensitive they are to local damage.

Colombo et al. [49] presented an inverse finite element method (iFEM) which is used to derive a novel feature for anomaly identification. To build a load-adaptive baseline that is simple to use in damage identification scenarios, the iFEM's capability to reconstruct structure deformations based on input strain data at discrete places without any a priori training or prior knowledge of the acting loads is employed. The load-adaptive baseline is based on an anomaly index that contrasts the strain measured by a test sensor in the same spot with the strain reconstructed by the iFEM at select test locations to highlight the structure's real state of health. The two values match when the studied structure is in a "healthy" condition; otherwise, they do not.

Due to requirements like comprehensive measured data and modal information needed before and after damaged states, classic damage detection methods are constrained in their practical applicability. Li et al. [50] mentioned that strain damage indexes have attracted wide attention due to their high sensitivity to local damage. For the purpose of reconstructing structural deformation, the displacement field based on the iFEM is obtained using the four-node inverse shell element (iQS4). Additionally, the strain field data is used to create the direct damage index, which detects damage under various damaged conditions. It improves the deficiencies of conventional damage identification techniques.

Perera et al. [51] proposed a comparison study between Multi-objective Particle Swarm Optimization (MOPSO) method and Strength Pareto Genetic Algorithm (SPGA) for solving multi-objective damage identification problems based on model updating methods and modal tests when modelling errors are present. The better quality of Pareto fronts obtained by the MOPSO algorithm as compared with the SPGA method is attributed to the specific combination of established as well as the novel multi-objective tools utilized. Additionally, the proposed MOPSO method has proven to be superior to the SPGA method.

In general, in the past two decades, studies related damage identification met a lot of success [52-56]. However, the traditional damage identification methods based on vibration characteristics have limitations on determining the damage shape and size. It is also restricted in the practical applications, due to factors including the complete measured data and modal information required before and after damaged states.

2.5 T-peel Joint

A T-peel joint is a special case within peel structures, normally formed by the adhesion of two bent objects. It is a common structure in adhesive and welding manufacturing. Most of the current studies of T-peel joints focus on determination of the strength of the joint by T-peel test. Generally, the peel force is applied in the direction normal to the adhesive surface along the bent objects. ASTM published a test method for T-peel test in1876 and has continued to update it until the present day [57].

Since the development of finite element method and computer aided analysis, the analysis of T-peel tests has relied on finite element analysis. Hinopoulos, George and William R. Broughton [58] presented an evaluation of the T-peel joint by using finite element analysis based on ABAQUS. The study focuses on the effects of environmental conditions and various geometric parameters on the performance and stress distribution within the adhesive joint in finite element analysis. It includes the influence of adhesive water content, adherend material characteristics, thickness, and the bent radius. The study also shows that while the T-peel test is beneficial for evaluating the peel resistance of adhesives and the environmental durability of adhesive systems, it has limitations, such as being restricted to thin and flexible adherends and not considering large deformations.

Optical measurement has also been widely used in T-peel tests. Ben Khalifa, et al. employed [59] Digital Image Correlation (DIC) technology for detailed strain and displacement measurements at the weld seams during the peel tests. This approach facilitated a comprehensive investigation of the mechanical properties and reliability of ultrasonically welded and soldered copper cable joints.

Fracture analysis is a vital topic in T-peel test. Hadavinia, H., et al. [60] presented a detailed examination of the adhesive fracture energy derived from both elastic-plastic and linear elastic fracture mechanics methodologies. In Ulrich Eitner and Carlos Li's study [61], measured peel forces were translated into adhesive fracture energies. This parameter is geometry-independent and quantifies the energy required to break interfacial bonds at the peel front, thus offering a more reliable measure of adhesive quality. Dai, Yanwei, et al. [62] proposed a study about how the sizes of pre-notches and pre-cracks affect the T-peel test results. The study utilizes a combination of experimental tests and the modeling of adhesive region to analyze the impact of these defects on fracture toughness, peak loads, and the transition from non-steady-state to steady-state peeling in ductile adhesive joints.

In recent years, research on T-peel tests has increasingly focused on the performance of specific material combinations and new materials within T-peel joints [63-66].

CHAPTER THREE

METHODOLOGY

Contact problems are represented the insufficient boundary problems to be served as the methodology study. A normal contact problem between two bodies A and B in a plane elasticity setting is shown in Figure 1. For brevity, symmetry is assumed in which body A is a round object while body B is a half elastic plane. Further, at the early stage of the development, the friction between the contact objects is ignored and both bodies undergo elastic deformation. Let the contact pressure in the contact region (CR) be $\sigma(x)$, where x designates the distance measured from the middle of the contact region as shown. In general, the free region (FR) is a free surface available for empirical measurements by an optical mean, for example.

Let $v\ (x, y)$ be the displacement of the object in the y-direction. In this study, the displacement on a few surface points is available for the following numerical implementation. It is clear that the two objects of concern are subject to an equal and opposite contact load along the contact region aside from other external loads outside of the contact region. The proof of the uniqueness solution of the problem is provided in Appendix B. In the proposed numerical scheme, only one body is slated for analysis which is designated as body B in Figure 1. It is the aim of the technique to determine the contact pressure on the body. Let the contact pressure in the CR be $\sigma(x)$ and the measured displacement on the free surface of body B be $\bar{v}(x) = v(x, 0)$.

Empirical determination of the contact pressure directly remains an extremely challenging task due to mainly the difficulty in accessing the obscured contact region.

[67-71] On the contrary the measurement of surface displacement can be easily achieved

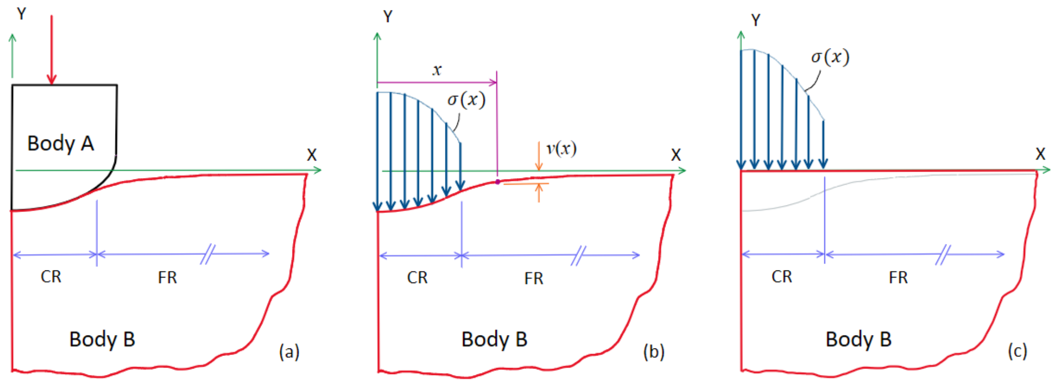

Figure 1. (a) A frictionless contact between two bodies A and B. (b) Contact stress σ(x) and y-displacement on the free surface v(x), and (c) a "forward" problem with applied load σ(x).

by optical means [72-75]. In view of the above-mentioned facts, this study proposes a new inverse method to determine the contact pressure as well as the size of CR, if it is unknown, based on a finite element model incorporating the measured displacement along the FR by an optimization scheme.

The logical flow chart is shown in Figure 2. In the first step the FE model for body B is created considering that *y*-displacements at a selected few node in FR are available. In the model an assumed pressure $\sigma_i(x)$ is applied. The finite element model is solved yielding the nodal *x*- and *y*-displacements, (u_i, v_i), at all the nodes. Finally, an error function is established to compare the FEA results of v_o with the measured $\bar{v}(x)$. The optimization process continues until the minimization criterion is reached.

To ease the computational complexity as depicted in Figure 2, the following simplification scheme is employed on the contact pressure $\sigma(x)$. Instead of a smooth and continuous function, the following two simplified functions are used. The first is a piecewise linear function defined as follows.

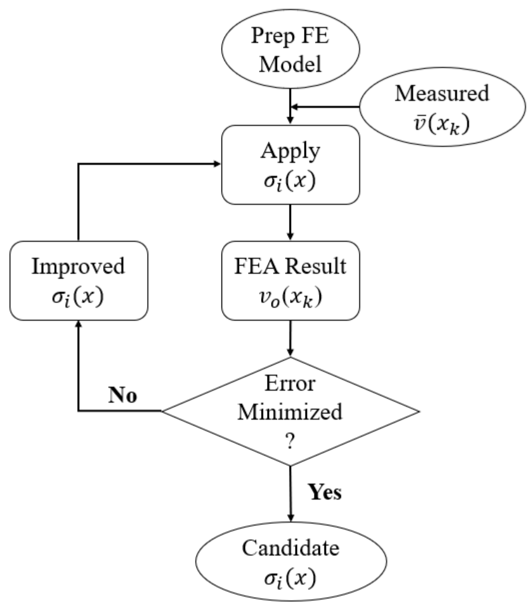

Figure 2. Flow chart.

$$f(x) = p_i + \frac{p_{i+1} - p_i}{x_{i+1} - x_i}(x - x_i), \qquad x_i \leq x \leq x_{i+1}, \tag{1}$$

where, as depicted in Figure 3, p_i and p_{i+1} are the unknown contact pressure at x_i and x_{i+1}. The second is a "staircase" function with each step described by the following equation.

$$g(x) = p_j\left[U\left(x - x_j\right) - U\left(x - x_{j+1}\right)\right], \qquad x_j \leq x \leq x_{j+1}, \tag{2}$$

where $U(x)$ is the usual Heaviside step function.

In the proposed hybrid numerical scheme, a finite element model of the elastic body with measured surface displacements is constructed yielding the following system of equations.

$$\mathbf{KU} = \mathbf{F}(p_j), \tag{3}$$

where **K** is the n-by-n stiffness matrix of the model, **U** the nodal displacement vector and p_j the applied pressure as indicated in Eqns. (1) and (2). The consistent nodal force vector from the surface traction **F** can be formed with ease following the usual fashion described in a standard finite element text such as [76, 77].

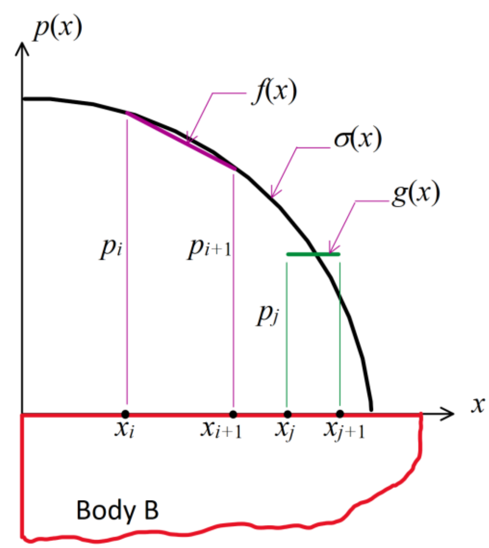

Figure 3. Approximation of applied pressure σ(x) using step function in $g(x)$ and piecewise linear function in $f(x)$.

Let the measured surface y-displacement at a set of α selected nodes be $\bar{v}_i$, $i = 1 \ldots \alpha$. The corresponding y-displacement found from solving Eqn.(3) is v_i which is given as follows.

$$\{\boldsymbol{v_i}\} = \mathbf{AU} = \mathbf{AK}^{-1}\mathbf{F}(p_j), \tag{4}$$

where **A** is a transformation matrix of size α-by-n consisting of mainly 0 and one 1 per row of α rows. For example,

$$\mathbf{A} = \begin{bmatrix} 0 & 0 & 0 & 0 & 0 & 1 \\ 0 & 0 & 0 \ldots 1 & 0 & 0 \\ 1 & 0 & 0 & 0 & 0 & 0 \\ & & \vdots & & & \\ & & \vdots & & & \end{bmatrix}. \tag{5}$$

The proposed hybrid method involves minimizing the difference between the numerical solution v_i and the experimentally measured displacement $\bar{v}_{\mathrm{i}}$. To this aim, an error function is defined as

$$e = \sum_{i=1}^{\alpha} \frac{1}{2} \|\bar{v}_i - v_i\|^2 = \sum_{i=1}^{\alpha} \frac{1}{2} \left\| \bar{v}_i - \left\{ \mathbf{AK}^{-1}\mathbf{F}(p_j) \right\}_i \right\|^2, \tag{6}$$

where $\|.\|$ represents the Euclidian norm of a vector. Therefore, the unknown contact pressure p_j can be found by solving the following minimization problem.

$$\min_{p_j} \sum_{i=1}^{\alpha} \frac{1}{2} \left\| \bar{v}_i - \left\{ \mathbf{AK}^{-1}\mathbf{F}(p_j) \right\}_i \right\|^2, \tag{7}$$

In addition, we seek a constraint on the minimization of the error function. In general, the knowledge of the applied force is available beforehand. This is to say,

$$F = \int p(x)dx, \tag{8}$$

After a simple discretization using β intervals, the above equation becomes,

$$\bar{F} = \sum_{j=0}^{\beta} p_j \Delta x_j, \tag{9}$$

where $\bar{F}$ is the known applied force and $\Delta x_j = x_{j+1} - x_j$. This numerical integration actually follows the step function indicated in Eqn. (2). Trapezoidal rule [78] to evaluate the integral may also be employed using the piecewise linear function given in Eqn. (1).

Alternatively, equivalent to the above constraint we may consider the reaction in the y-direction at the supporting edges of the model. Let R_{yj} be the reaction in the y-direction at the j-th node on the supporting boundary. Then we have the following constraint,

$$\bar{F} = R \equiv \sum_j R_{yj}, \tag{10}$$

which is not as explicit a constraint in p_j as seen in Eqn. (9). For some instances problem specific constraints may exist. They will be disclosed in the following sections. Note that both constraints may be written in a more general form called constraint equation $C = 0$ after moving the right-hand-side term to the left. Consequently, we have the following constrained minimization problem,

$$\min_{p_j} \sum_{i=1}^{\alpha} \frac{1}{2} \left\| \bar{v}_i - \left\{ \mathbf{AK}^{-1}\mathbf{F}(p_j) \right\}_i \right\|^2, \tag{11}$$

subject to,

$$C \equiv \sum p_j \Delta x_j - \bar{F} = 0. \tag{12}$$

There are abundant methods [79-82] for solving the above constrained minimization problem. For example, the error function may be modified to include a Lagrange's multiplier term incorporating the constraint [83]. Taking the gradient of the modified error function yields a system of nonlinear equations which may then be solved by the regular Newton-Raphson iteration [84]. In this study, Nonlinear Programming by Quadratic Lagrangian, or NLPQL for short [85, 86], is chosen to solve the constrained minimization problem.

NLPQL is a FORTRAN implementation first published by Schittkowski [87, 88] which can be called directly by most of FORTRAN based commercial software, such as ANSYS, Design Xplorer, TOMLAB, etc. It is for solving nonlinearly constrained optimization problems by a sequential quadratic programming (SQP) algorithm. A general optimization problem consists of minimization of a differentiable objective function subject to nonlinear equality and inequality constraints functions. There are also some necessary assumptions for sequential quadratic programming:

- The problem is smooth which means the problem functions are continuously differentiable on its definition domain.
- The problem is not too large. Based on Schittkowski's study, NLPQL is tested extensively on problems with up to 100 variables.

In the current study, the objective function is given in Eqn. (11) and the constraints are given in Eqns. (12).In this study, the problem is relatively small in which there are only 5 to 15 variables. The NLPQL also needs a set of initial values of all the variables to start the program. The initial value can be picked arbitrarily; however it is with a high possibility that it will lead a the NLPQL program be immersed into a wrong region of the local solution and miss the correct solution. Thus, a proper set of initial value of all the variables is necessary to be determined and to be fed into the NLPQL program. To seek the initial values, we can use a global optimization method with acceptable samples, i.e., screening method which uses a simple approach based on sampling and sorting. It is usually used for global behavior study. The number of samples for the global optimization method used in this study is from 100 to 2000.

In the following chapters seven examples are selected to demonstrate the effectiveness and accuracy of the proposed methodology. The first example is a thin plate bending problem which provides a simple demonstration of the methodology. The second example to the fourth example is the application and the verification on several contact problems. The last three involve some other types of insufficient boundary problems, one is a single lap problem, one is a damage identification problem on a cantilever beam, and the last one is based on T-peel test.

CHAPTER FOUR

THIN PLATE BENDING

4.1 Problem Description

An ordinary thin plate bending problem is studied to demonstrate the new method. A thin plate with 1mm in thickness, 60 mm in length and 200 mm in width is depicted in the sectional view as shown in Figure 4. The thin plate is fixed at the two sides with applied pressure $\sigma(x)$ distributed symmetrically at the middle of the plate. A symmetric plane strain model is employed for the study. Further, the material of the plate is aluminum alloy Young's modulus $E = 71$ GPa and Poisson's ratio $\nu = 0.3$.

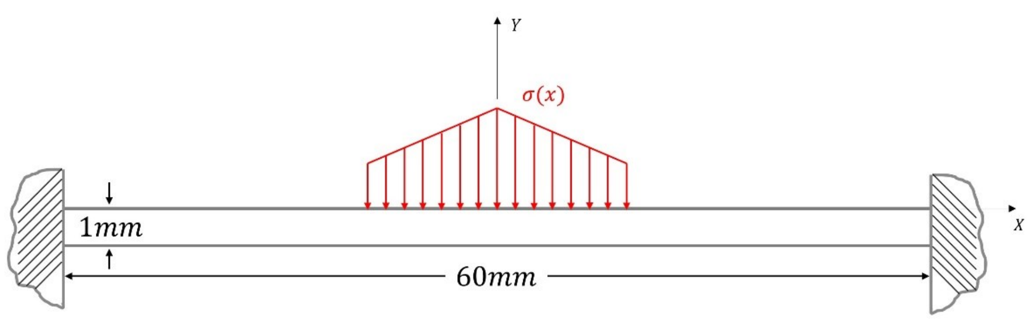

Figure 4. Schematic for beam.

The finite element mesh for the plate is shown in Figure 5. The thin plate is meshed with a size of 0.2 mm. The edge on the *y*-axis is constrained against the movement in the *x*-direction as if it has a frictionless contact with a rigid surface. Further, the right edge of the plate is fixed rigidly. A distributed pressure $\sigma(x) = (1.5 -$

$0.125x$) MPa is applied in $0 \leq x \leq 8$ mm. At the current stage of developing the novel technique, numerically simulated y-displacements at nodes on the top edge of the plate from 8 mm $\leq x \leq 30$ mm are used in place of the actual experimental measurement. The software ANSYS is adopted to calculate the required y-displacements using the mesh shown in Figure 5.

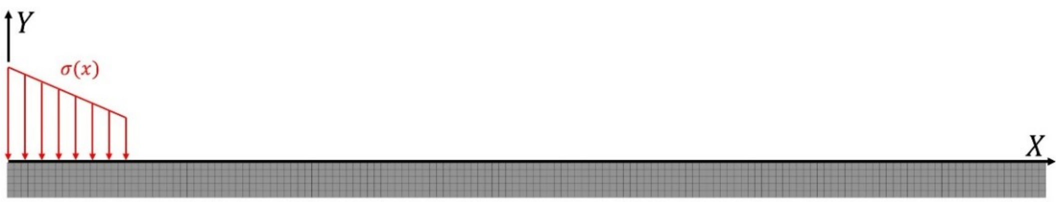

Figure 5. Finite element mesh.

<u>4.2 Result and Algorithm Evolution</u>

Because of the simple geometry and the linear load, the optimization parameters are rather simple in that the unknown variables chosen are p_1 at $x = 0$ and p_2 at $x = 8$ mm to be used in Eqn. (1). Further, the lower bound of the two variables is 0 and the upper bound is 4. As depicted in Figure 6, there are 5 equally spaced points selected in the free region whose simulated y-displacements, $\bar{v}_i$ are used as empirical measurements in the proposed numerical scheme. Note that $\bar{v}_1$is at $x = 10\ mm$.

The solutions are solved by different optimization methods under different constraint conditions. The effectiveness of the optimization method and the constraint conditions are also studied in this section. Proof by exhaustion is the most basic way to find the best solution from mass data. With sufficient iteration steps, it can solve the

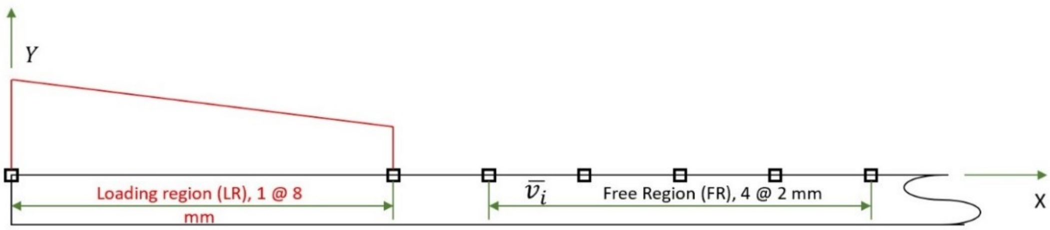

Figure 6. Selection of points on free region (FR) with known y-displacements.

problem indisputably, but with extremely long computation. As shown in Figure 7 (the values in Figure 7 are for references only, they are not real), optimization method can effectively reduce the requirement of the quantity of the data. However, the number of computation steps might still be massive.

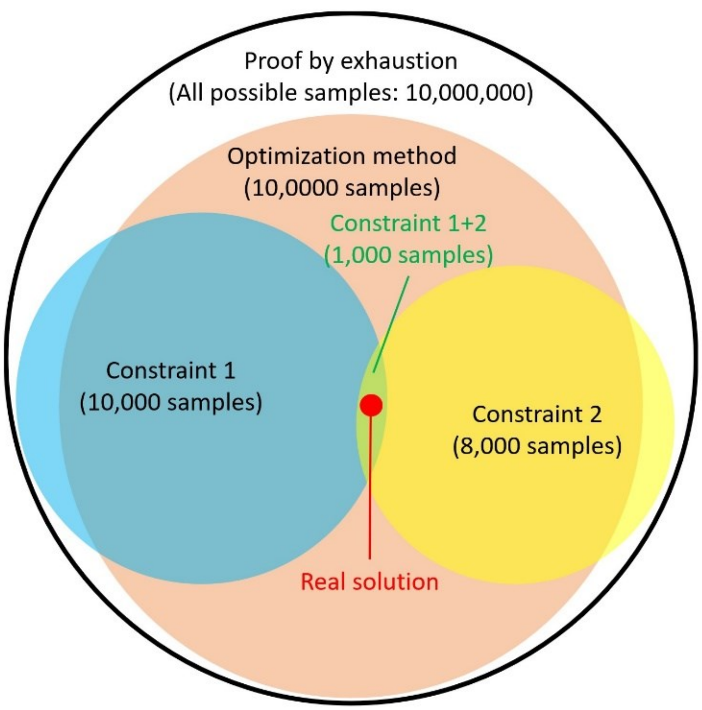

Figure 7. Comparison between each optimization method.

To make the optimization more efficient, constraint conditions must be involved. Two constraint conditions which might be known are imposed as follows: $p_1 \geq p_2$, and $4(p_1 + p_2) = 8$. Note that $4(p_1 + p_2)$ is the equivalent force R per unite width of the total applied loading. The accuracy and the quantity of the samples are compared. A group of samples is a unique combination of p_1 and p_2. For example, if the precision of the variables is 0.01, for the method of exhaustion, each variable has 400 possible values. Further, the quantity of the samples is 160000. The quantity of samples for each method represents the quantity of the computation steps. As Table 1 depicts, proof by exhaustion can solve the problem accurately, but the quantity of samples is extreme large. Further, by using optimization method under both constraint conditions, the problem can be solved in 118 samples with 99.999% accuracy. From the comparison between the solution by the optimization without constraint and the solution with constraint, the result accuracy can be increased by increasing the quantity of samples.

Table 1. Results and iteration steps of example 1.

			Optimization				
Parameters	Theoretical	Proof by exhaustion (0.01)	No constraint		Constraint 1		Constraint 1&2
Samples	N/A	160000	280	2114	138	447	118
p_1 (MPa)	1.5	1.5	1.128	1.5	1.427	1.506	1.5
p_2 (MPa)	0.5	0.5	0.886	0.5	0.576	0.496	0.5
Error (%)	0	0	0.0313	0	0.0069	3.6e-5	0
R (N)	8	8	8.058	8	8.011	7.999	8

CHAPTER FIVE

RIGID BLOCK CONTACTING AN ELASTIC PLATE

5.1 Problem Description

Figure 8 depicts the schematic of the problem to be studied using the proposed hybrid numerical-experimental scheme. More specifically, a rigid block is pressing on the edge of a semi-infinite elastic plate. It is chosen here primarily because the theoretical solution of the contact stress is provided in the text by Roark and Young [89]. For a point Q at x on the edge of the elastic plate, the contact stress $\sigma(x)$ is given as follows.

$$\sigma(x) = \frac{2P}{\pi t\sqrt{b^2 - x^2}} \tag{13}$$

where t is the thickness of the plate and the definitions of the remaining variables are given in Figure 8. Note that the force $2P$ is seen in Eqn. (13) because a symmetric model is to be used in the numerical study.

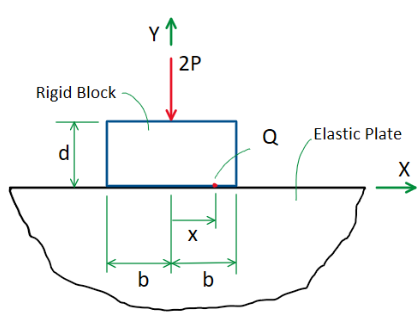

Figure 8. Schematic for example 2.

A symmetric plane stress model is employed for the study in which the following geometric values are chosen for the rigid block: $b \times d = 10 \text{ mm} \times 10 \text{ mm}$, and for the elastic plate: 30 mm × 30 mm, and t = 1.0 mm. Further, the material properties for the elastic plate are: Young's modulus E_p = 2 GPa, Poisson's ratio ν = 0.3. The Young's modulus of the rigid block is chosen to be $E_b = 10^3 \times E_p$. Note that, as depicted in Eqn. (13), the contact pressure is independent of material constants. As evidenced in the later analysis, the size chosen for the semi-infinite plate is rather adequate.

The finite element mesh for the two bodies is shown in Figure 9. The top edge of the plate is meshed into divisions of size 0.1 mm. As in the common practice for a symmetric model, the edges on the y-axis are constrained against the movement in the x-direction. Further, the bottom edge of the elastic plate is fixed rigidly. A force P = 400 N in the negative y-direction is applied on the top edge of the rigid block. Frictionless contact is also assumed between the two objects. Only the mesh for the elastic plate is included in the proposed numerical scheme. Furthermore, in order to accommodate the constraint equations an extensive ANSYS APDL code [90] must be developed.

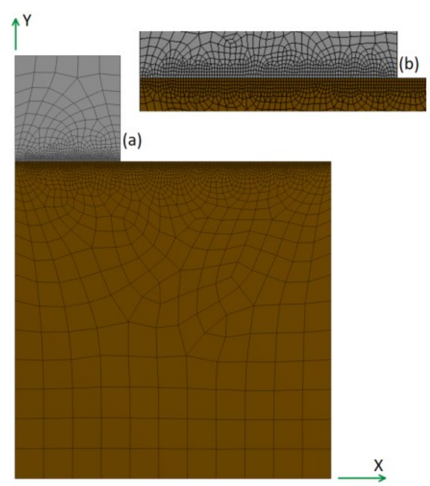

Figure 9. (a) Finite element mesh and (b) close-up of mesh at contact of a rigid block pressing an elastic plate.

5.2 Result and Algorithm Evolution

As depicted in Figure 10, there are 10 points selected in the free region whose simulated *y*-displacements, $\bar{v}_i$ with $\bar{v}_1$ at $x = 12$ mm, are used as empirical measurements in the proposed numerical scheme. Further there are ten spans of equal size in the contact region within which the contact pressure, p_j, are to be determined. The contact region is also discretized into different number of divisions to study the effect of the discretization of the contact region. Thus, both α and β in Eqns. (6) and (9) are equal to 10. Note that p_0 is the contact pressure at $x = 0$.

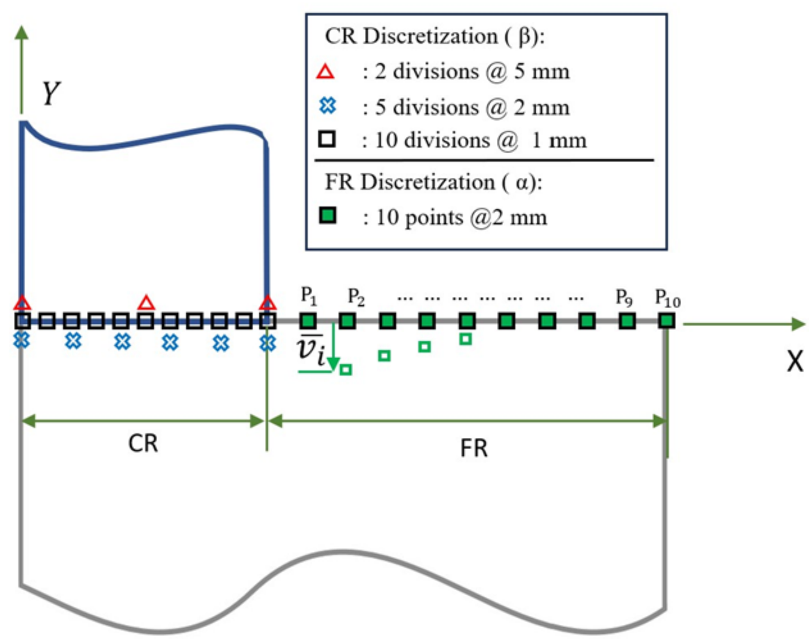

Figure 10. Selection of points on free region (FR) with known y-displacements.

It is found that the "solution" for the contact pressure p_j is poor in accuracy compared to the theoretical counterpart given in Eqn. (13), although a large number of iterations and CPU time are exhausted. The solution did exhibit a subtle trend of monotonicity. That is, p_j increases as x becomes larger which is typical in many contact problems involving rigid bodies with sharp corners [4]. Consequently, the following constraint is implemented in the algorithm to ensure a monotonic contact pressure.

$$p_j(x_j) \le p_{j+1}(x_{j+1}), \qquad x_j < x_{j+1} \tag{14}$$

Obviously no converged solution is achieved provided that the reverse relation of Eqn. (14) is considered in the algorithm. Another obvious constraint which needs to be included in the beginning is that the contact pressure is always non-negative since there is no bonding agent between the two contacting bodies. Thus,

$$p_j(x_j) \ge 0 \tag{15}$$

Consider this evolving numerical algorithm with the added constraints a learning process. With both additional constraints implemented in the algorithm, the problem comprising of Eqns. (11), (12), (14) and (15) is solved again. Define the average relative error ϵ as follows.

$$\epsilon = \frac{1}{\alpha}\sum_{i=1}^{\alpha}\left|1 - \frac{v_i}{\bar{v}_i}\right|, \tag{16}$$

Table 2 shows the calculated average relative error ϵ and reaction force R under two approximations for the contact pressure $p(x)$. Note that the applied force is 400 N. It is readily seen that the calculated results are extremely accurate as far as satisfying the specified constraints is concerned. Note that, as expected, the performance of using the piecewise linear function holds an upper hand over the one approximated by step functions. From the numerical experiment, it is found that constraint equation Eqn. (14) plays a more important role than Eqn. (12). Namely the solution set reached by relaxing the constraint Eqn. (12) deviates almost unnoticeably from the set reported in Table 2.

Table 2. Computed average relative error ϵ and reaction force R of example 2.

$p(x)$ Approximation	ϵ (%)	R (N)
Step Function *g(x)*	0.24	390.7865
Piecewise Linear *f(x)*	0.07	400.0136

Figure 11 depicts the theoretical contact pressure as given in Eqn. (13) and the one calculated using the finite element mesh seen in Figure 9. The two curves (dashed and dotted) nearly coincide with each other, thus indistinguishable. This validates the mesh quality used in the numerical study.

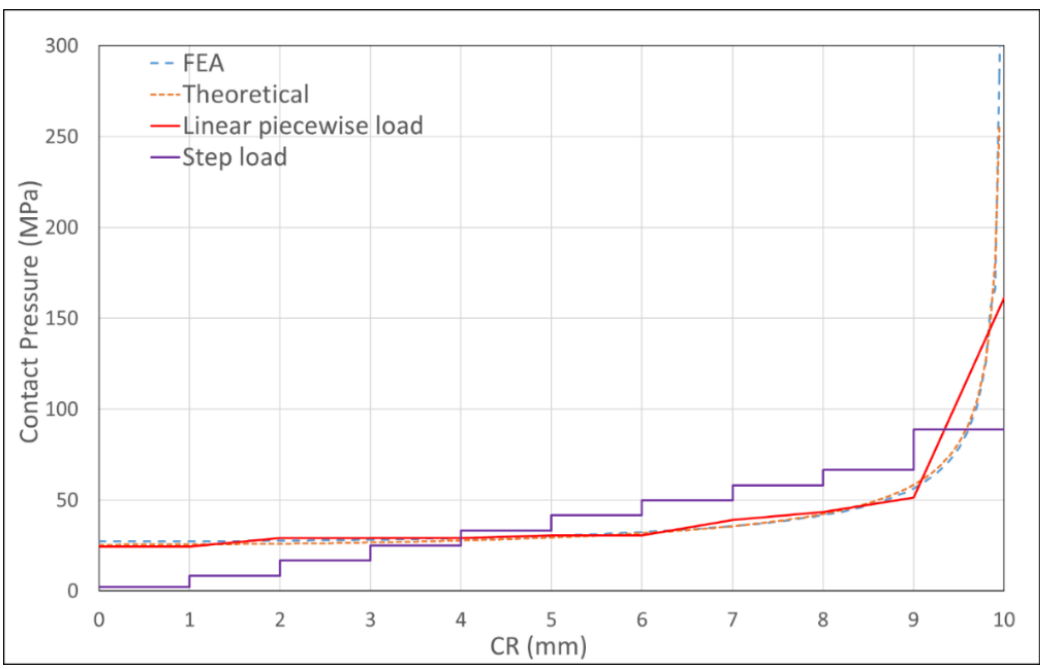

Figure 11. Calculated contact pressure for example 2.

Also depicted in Figure 11 is the calculated contact pressure based on the proposed technique with some measured or simulated surface displacements embedded in the algorithm. It is seen that the predicted contact pressure using step-function approximation is underestimated near the center of the contact region. However, it is overestimated on the outer half of the whole contact region.

It needs to be noted that there exists a singularity in $p(x)$ at the outer edge of the rigid block, $x = b$, as evidenced in Eqn. (13). It is a common feature in contact problems involving an object with sharp corners [4]. As seen in Figure 11, when the contact pressure is approximated by piecewise linear functions, the calculated contact pressure using the evolved numerical algorithm is in excellent agreement with the theoretical solution until near the edge of the block where the contact pressure rises to infinity.

There are some factors that may affect the solution accuracy, such as the discretization size along the contact region, the overall mesh size of the model, the number of known displacements along the free region, etc. In addition, the embedded empirical errors in the displacements along the free surface also plays an important role in obtaining an accurate solution. The following study shows the effect on the accuracy of the solution due to the introduction of an artificial noise into the known displacements. Let η be the percentage of random artificial error imposed on the known displacements. Therefore, the contaminated data to be fed into the proposed numerical algorithm is expressed as $\bar{\bar{v}}_i = (1+\eta)\bar{v}_i$. Using various combinations of parameters, α, β, Δ, and η, in solving Eqn. (11) subject to constraints Eqns. (12), (14) and (15), the calculated average relative error ϵ and reaction force R are given in Table 2. Note that the piecewise linear function as given in Eqn. (2) is used.

Table 3. Results of the study of accuracy influencing factors of example 2.

Case#	α	β	Δ (mm)	η (%)	ϵ (%)	R (N)
1	10	10	0.1	0	0.071	400.014
2	10	10	1.0	0	0.096	395.683
3	10	2	0.1	0	0.341	400.000
4	10	5	0.1	0	0.214	400.500
5	3	10	0.1	0	0.186	383.506
6	5	10	0.1	0	0.152	391.443
7	10	10	0.1	± 1.5	0.596	396.244

Figure 12 shows the computed contact pressure using the seven cases listed in Table 3. Figure 12 (a) reveals that a model with finer mesh with $\Delta = 0.1$ mm provides more accurate results in contact pressure than the coarse counterpart with $\Delta = 1.0$ mm. Figure 12 (b) depicts that with more divisions used along the contact region, the predicted contact pressure approaches more closely to the theoretical pressure.

The sensitivity of the number of the known displacements is demonstrated by using three points marked as P_1, P_3, and P_5, and five points marked as P_1, P_3, P_5, P_7, and P_9 in Figure 10 corresponding to $\alpha = 3$ and 5 in Eqns. (16), respectively. The computed contact pressures are shown in Figure 12 (c). This conforms with the general consensus that more known data produces more accurate results. Finally, the effect on the predicted pressure due to the error embedded in the known displacement along the free region is considered. To this end, random errors of $-1.5\% \leq \eta \leq 1.5\%$ are added to the displacements ($\bar{v}_i$) of the 10 points marked as P_1 to P_{10} in Figure 10 following Eqn.(16). The relative error ϵ reported in Table 3 is calculated using $\bar{\bar{v}}_i$ in place of $\bar{v}_i$. It is seen from Figure 12 (d) that the effect of the noise is not as severe as in other ill-posed problems [91].

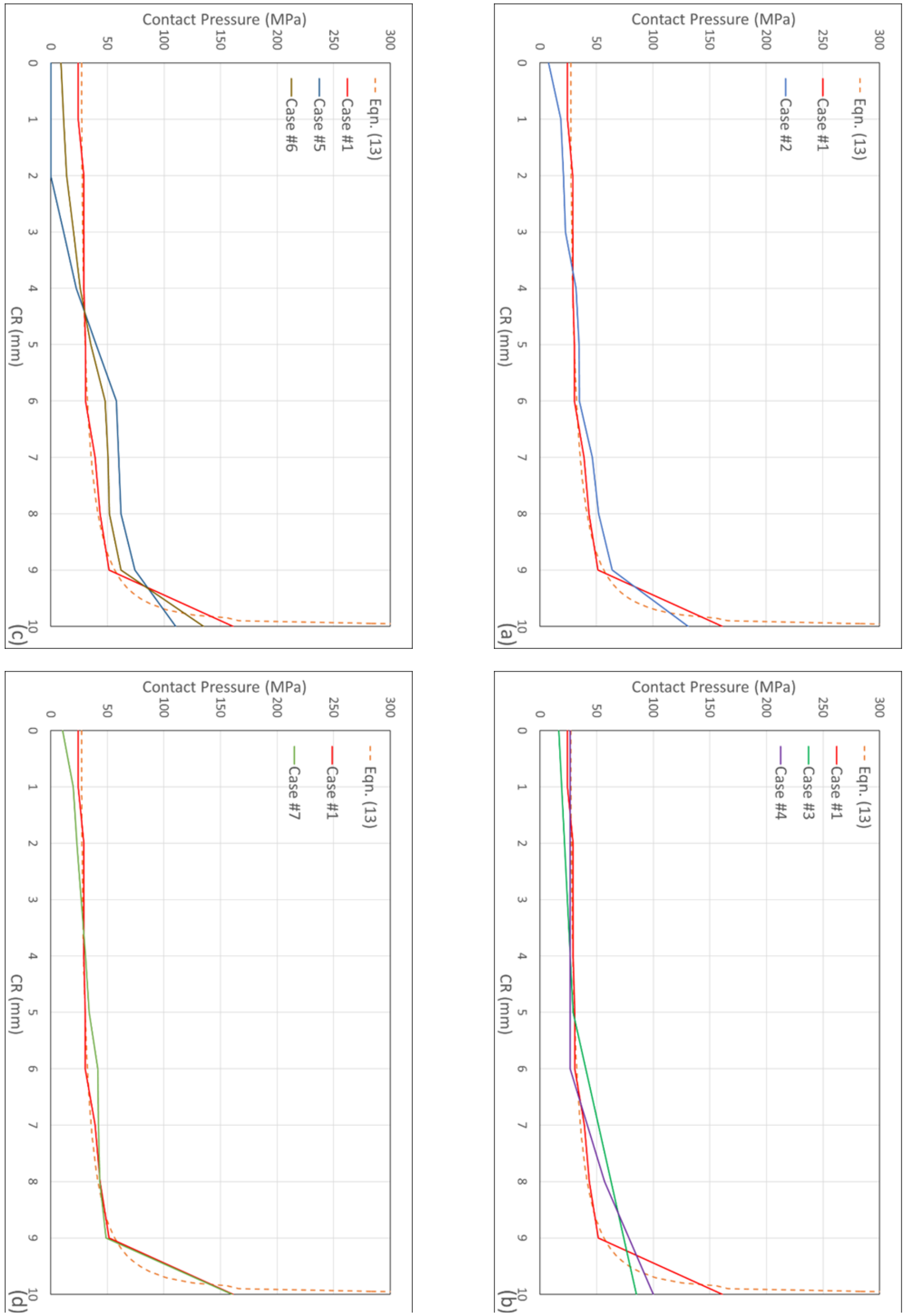

Figure 12. Theoretical vs. calculated contact pressure using various sets of parameters in Table 3.

CHAPTER SIX

WASHER IN A BOLT JOINT

6.1 Problem Description

One of the most common methods in joining parts in automotive industries is to use bolt-washer-nut mechanism. The inset in Figure 13 shows that only three components – bolt, washer and base – are included in this study. A second object to be joined with the base and the nut are excluded. Further The size of the base is relatively large compared to the bolt and washer. Thus only a round portion of the base is selected. In addition, the bolt is assumed to have a round head as well. The threads of the bolt may exists at the lower end and are neglected in the study. As a result, an axisymmetric model is a suitable practice. Figure 13 shows the sectional view of the components as well as the nomenclature of the parameters used in the following numerical analysis.

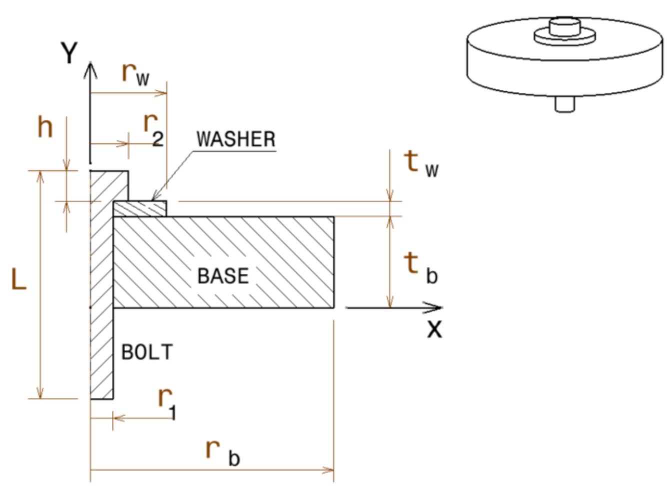

Figure 13. Sectional view of a bolt joint assembly consisting of a bolt, a washer and a base seen in inset.

The finite element mesh seen in Figure 14 is created according to the following choice of parameter values referring to the nomenclature given in Figure 13: [BOLT] r_1 = 3.0 mm; r_2 = 6.4 mm; h = 6 mm; L = 25 mm, [WASHER] r_w = 10.0 mm; t_w = 1.0 mm, and [BASE] r_b = 43.0 mm; t_b = 15.0 mm. Note that the radius of the holes in the washer and base body are the same as the radius of the bolt. Further, steel with Young's modulus E_s = 200 GPa and Poisson's ratio ν_s = 0.3 is selected for the bolt and washer while the base is of aluminum with E_a = 71 GPa and ν_a = 0.3. The axial force applied at the lower end of the bolt is P = 1000 N.

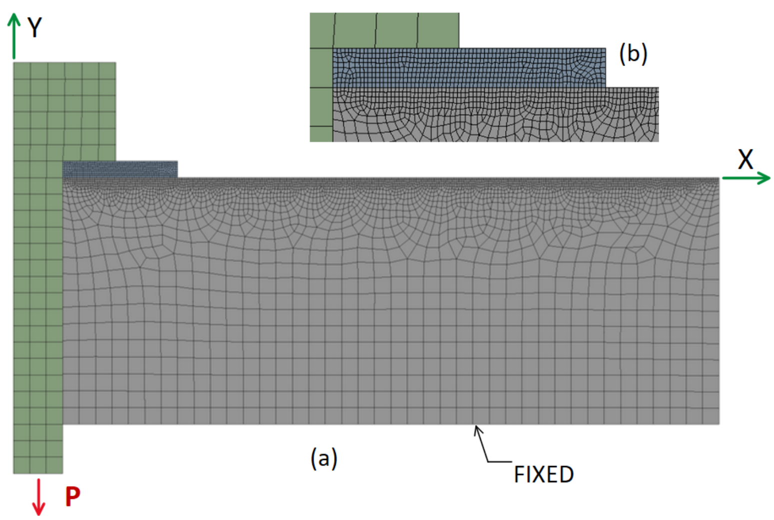

Figure 14. (a) Axisymmetric FE mesh, (b) close-up along contact.

The goal is to determine the contact pressure between the washer and the base using the proposed numerical technique, thus warranting a fine mesh along the contact regions. As opposed to the previous example where a rigid block is present, the current example involves two deformable bodies. It is highly plausible that there exists an uplift near the right end of the washer as depicted in Figure 15(a) where the contact between the two objects ceases at point Q. Consequently, the following treatment is provided to the contact region.

The selection of points in the free region (FR) whose y-displacements $\bar{v}_i$ are to be fed into the proposed numerical scheme is addressed first. As shown in Figure 15(b), there are nine points selected which are split into three groups denoted by FR_1, FR_2 and FR_3 with 0.5 mm, 0.7 mm and 1.0 mm, respectively, for the sizes of the three equal segments in each group. It is a common practice in the fields of fault diagnosis and non-destructive-testing that the signals received closer to the zone to be scrutinized weigh more significantly than those farther away. This also explains why there is no point selected after FR_3, 16.6 mm $< x < r_b = 43$ mm, simply because the signals received are weak rendering insignificant effects on the analysis.

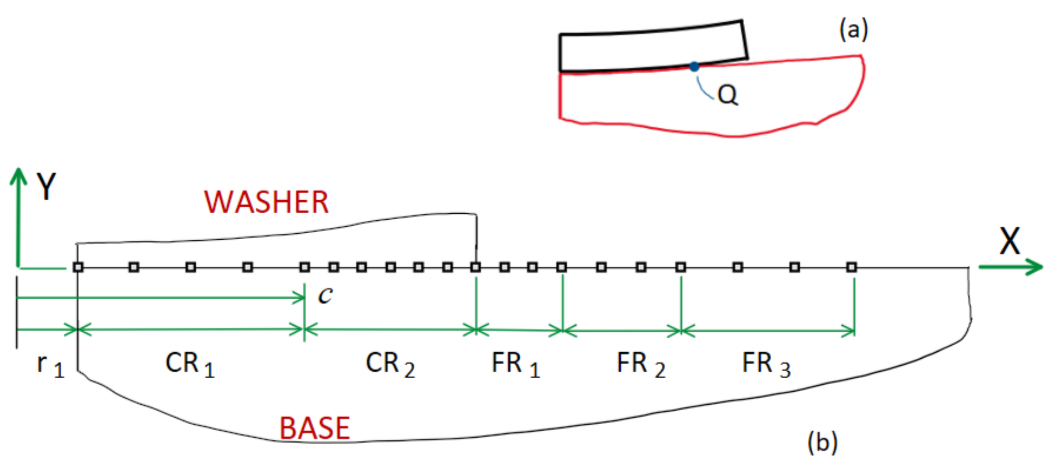

Figure 15. (a) Deformed washer and base, (b) discretization of contact and free regions.

As elaborated previously, the size of the contact region is not known *a priori*. The whole region is split into two – one with larger size in CR_1 and the other with a fine size in CR_2 in order to precisely pinpoint the location of the margin of the contact region. This is in analogy to using a fine mesh to secure a critical stress in a loaded machine part. In light of the previous example, contact pressure approximated by step functions tends to yield poor results. Thus for each segment in both CR_1 and CR_2 piecewise linear functions are used to represent the contact pressure as put forth in Eqn. (1).

6.2 Result and Algorithm Evolution

For the current contact problem, the theoretical solution does not exist in literature after a thorough search. Therefore, only the simulation results, including the contact pressure and surface y-displacement, obtained by solving the model in Figure 14 are used as a reference for comparison in this section. To expedite the convergence and achieve a more accurate solution, in addition to the constraint equations in Eqn. (12) and (15), the following condition is also enforced after the failed attempt to find a solution under constraint Eqn. (14), the reverse relation of the following.

$$p_j(x_j) \geq p_{j+1}(x_{j+1}), \qquad x_j < x_{j+1} \tag{17}$$

Table 4 lists two sets of result of the average relative error ϵ and reaction force R found at the bottom edge of the aluminum base. It is readily seen that when the constraint imposed on the total reaction at the bottom edge of the aluminum base is enforced, the accuracy on the y-displacement on the free surface also improves somewhat.

Table 4. Computed average relative error ϵ and reaction force R of example3.

Eqn. (12) included	ϵ (%)	R (N)
No	0.041	1001.5
Yes	0.008	1000.1

Figure 16 shows the simulated contact pressure (in smooth solid line) in CR calculated using the model depicted in Figure 14. Note that the initial CR spans from x = 3 mm to 10 mm, the inner and outer radii of the washer, respectively. Due to uplifting of the washer, the contact pressure decreases monotonically and vanishes completely at x = 7.68 mm. This signifies the actual size of the CR.

Three configurations are used in the proposed numerical method to find the contact pressures all of which contain the 9 known y-displacements as depicted in Figure 15(b). In the first configuration, the entire CR is divided into ten equal parts, each being 0.7 mm in length. Every segment is given a piecewise linear pressure function. The calculated contact pressure is plotted in long dashed line against the simulated one. Although the calculated contact pressure deviates from the simulation significantly near x = 3 mm, the size of the CR is 7.9 mm, rather close to the simulated solution.

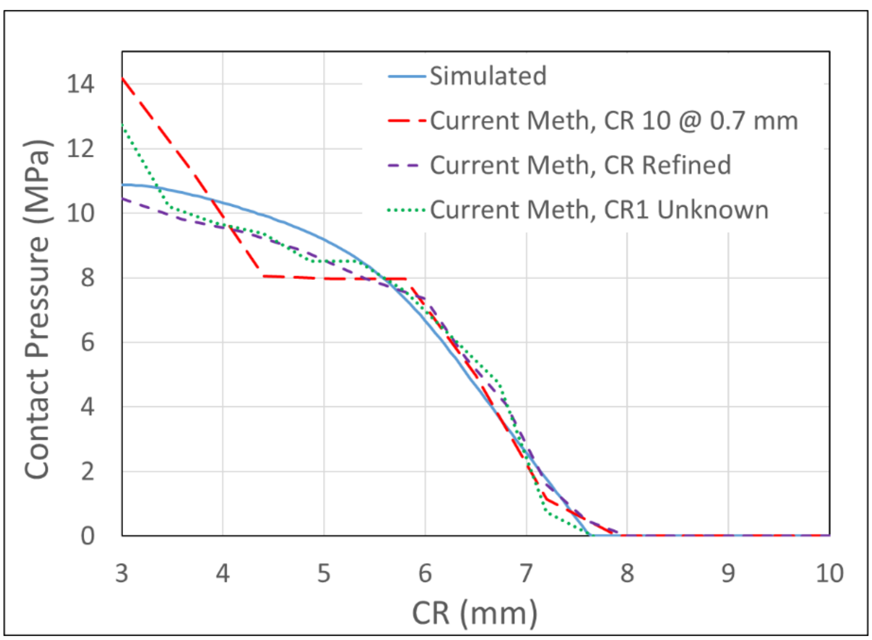

Figure 16. Simulated vs. calculated contact pressures for example 2.

To improve upon the previous configuration, the CR is split into two large divisions: 3 mm < $x \leq$ 6 mm, and 6 mm < $x \leq$ 10 mm, labeled as CR_1 and CR_2 in Figure 15(b). The length of the segments in the first division is set equal to 0.6 mm, while the segments are smaller in the second division. By iterating the size of the segments in CR_2, it allows the size of the contact region to be determined accurately. The predicted contact pressure using the refined segments is plotted in a short dashed line in Figure 16, which is in good agreement with the simulation. The size of the contact region, however, deviates further from the simulated result at 8.0 mm.

In the third configuration, a new unknown variable is introduced into the numerical framework, that is, the location where the contact pressure vanishes, labeled as c in Figure 15(b). Consequently, the minimization becomes as follows.

$$\min_{c,p_j} \sum_{i=1}^{\alpha} \frac{1}{2} \left\| \bar{v}_i - \left\{ \mathbf{A}\mathbf{K}^{-1}\mathbf{F}(p_j) \right\}_i \right\|^2 . \tag{18}$$

Therefore, unknown linear piecewise contact pressures in CR_1 are sought and CR_2 is treated as the extension of the FR in which the contact pressures are set equal to zero. The constraints continue to be valid in this new scheme. Additionally, there are ten equal subdivisions in CR_1 and they are of varying length depending on the value of c.

The predicted contact pressure using advanced configuration is plotted in a dotted line in Figure 16, which is in good agreement with the simulation overall, except near the inner edge of the washer. It is found that contact pressure vanishes at c = 7.66 mm, nearly identical to the simulated result. Note that smaller subdivisions for CR_1 can provide more accurate results, although the computation time will increase exponentially. It is worth noting that, for the last case, the computing time on a PC equipped with a CPU [11th Gen

Intel(R) Core (TM) i7-11800H @ 2.30GHz] and RAM size of 32 GB reaches up to 10 hours.

CHAPTER SEVEN

HERTZIAN CONTACT

7.1 Problem Description

In the well-known Hertzian contact problem, a cylinder is pressed against a block, as shown in Figure 17. The block can be assumed as a cylinder with infinite radius. For convenience, the length of the cylinder is set be equal to the thickness of the block. As result, a two-dimensional model is a suitable practice. The contact region between the two objects transforms a point into a line after the loading.

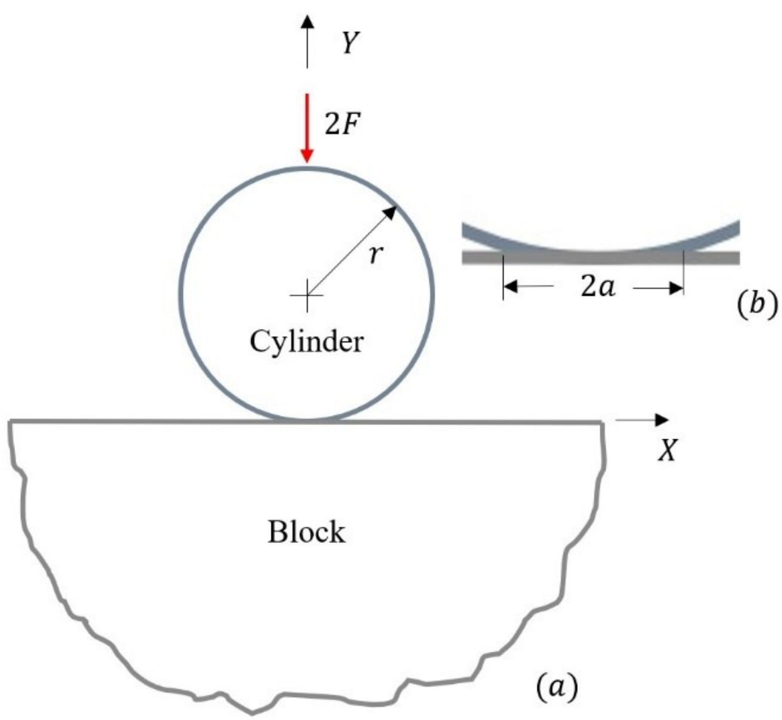

Figure 17. (a) Schematic for Hertzian contact problem between a cylinder and a block, (b) close up along contact.

The theoretical contact width and the contact pressure distribution are provided by Hertz's study [2]. Based on the coordinate system in Figure 17, the half contact width *a* is given as follows,

$$a = \sqrt{\frac{8FE^*}{\pi L/r}}. \qquad (19)$$

where *L* is the length of the cylinder, and for plane strain problems, *L=1.* The effective elasticity modulus E^* has the relationship with the elasticity moduli of the cylinder E_1 and the block E_2 given as,

$$\frac{1}{E^*} = \frac{1 - v_1^2}{E_1} + \frac{1 - v_2^2}{E_2} \qquad (20)$$

where v_1 and v_2 are the Poisson's ratios. The theoretical stress distribution $\sigma(x)$ is given as follows,

$$\sigma(x) = \frac{E^*}{2r}\sqrt{a^2 - x^2} \qquad (21)$$

The maximum contact pressure occurs at $x = 0$. A symmetric plane strain model is built for the simulation and the optimization. The following geometric values are chosen for the cylinder:$r = 100$ mm, and for the block: 120 mm $\times 120$ mm. Further, the material properties for the cylinder and the block are: Young's modulus $E_1 = E_2 =$ 20 GPa, and Poisson's ratio $v_1 = v_2 = 0.3$.

The finite element mesh for the two bodies is shown in Figure 18. A quarter model of the cylinder is employed for saving the storage and avoiding the insignificant computation. Because of the insufficient contact boundary, a potential contact region is selected from $x = 0$ to $x = 15$ mm. A fine mesh along the contact region is set for the analysis. The edges on the *y*-axis are constrained against the movement in the *x*-direction.

Further, the bottom edge of the block is fixed rigidly. A force $F = 400$ N in the negative y-direction is applied on the top edge of the cylinder. Frictionless contact is also assumed between the two objects. All the nodes from the top edge of the cylinder are coupled with the same movement in the y-direction.

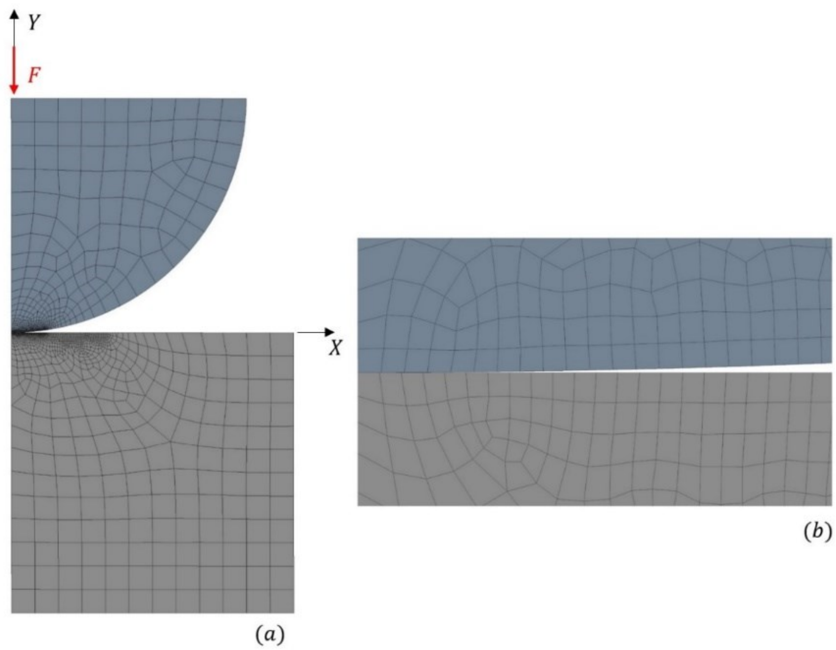

Figure 18. Hertzian contact problem between a cylinder and a block, (b) close up along contact.

As in the previous presented contact problems, the two deformable bodies contact along the CR as depicted in Figure 19. Only the mesh for the elastic plate is included in the proposed numerical scheme. The treatment of the CR and FR is followed: Due to the insufficient contact boundary, FR is defined as starting from $x = 20$ mm. There are ten points selected with equal segments. The y-displacements $\bar{v}_i$ for each point is to be fed into the proposed numerical scheme.

Two configurations are used under different schemes of CR. In the first configuration, CR contains 10 equal segments whose size is 1.5 mm. Similarly, as in the previous example, every segment is given a piecewise linear pressure function. Once the calculated contact pressure vanishes, the predicted contact region determined. In the second configuration, CR still contains 10 equal segments, but the length of the CR is set as a new variable c. The size of each segment is $c/10$. The contact pressure at $x = c$ is zero.

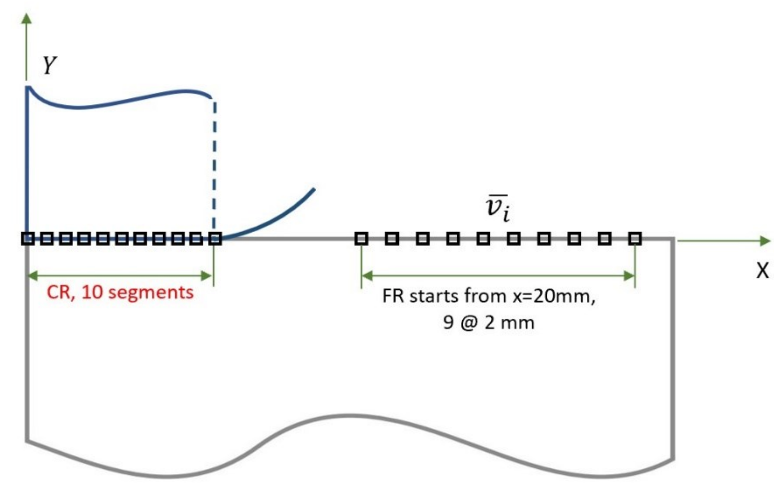

Figure 19. Discretization of contact and free regions.

7.2 Result and Algorithm Evolution

For the Hertzian contact problem, the theoretical solution, which includes the size of the contact region and the contact pressure, are calculated by using Eqns. (19) and (21). Because the effective of the constraint conditions are studied in the previous chapters, to expedite the convergence and achieve a more accurate solution, in addition to the constraint equations in Eqns. (12), (15) and (17). The comparison of the results will only be between the two configurations of the scheme of CR. The configuration 1 employs the Eqn. (11) for the minimization, and the minimization equation for configuration 2 is Eqn. (18).

Table 5 lists the result of the average relative error ϵ, reaction force R, and the length of the contact region a. The theoretical contact length is 9.627 mm, which has 3.7% difference from the simulation results. This might be caused by the limitation of the FEM. Due to the fact that $\bar{v}_i$ from FR is the results of the FEM, the deviation of the results is foreseeable.

Table 5. Computed average relative error ϵ, reaction force R and Contact length a of the Hertzian contact problem.

Method	ϵ (%)	R (N)	a (mm)
Theoretical	N/A	400	9.627
Simulation	N/A	400	9.857
Configuration 1, CR = 15 mm	0.0571	401.98	9
Configuration 2, CR is unknown	0.0309	400.41	9.556

Figure 20 depicts the contact pressure distribution along the CR. The theoretical pressure and the simulation pressure highly coincide with each other until $x > 9$ mm. The predicted contact pressures are in good agreement with the simulation and the theoretical overall. Configuration 2 has more accuracy than configuration 1 no matter for the length of the CR or the similarity to the theoretical contact pressure. However, configuration 1 and configuration 2 both lack of the accuracy of the highest pressure.

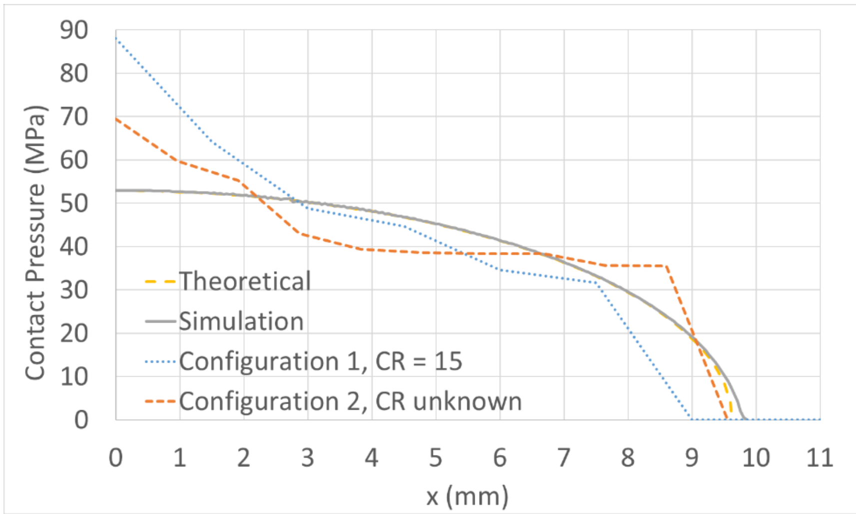

Figure 20. Theoretical and simulated contact pressure vs. calculated contact pressures for the Hertzian contact problem.

CHAPTER EIGHT

SINGLE LAP JOINT

8.1 Problem Description

Figure 21 depicts a single lap joint as a bounded problem. Further, two pieces aluminum sheet metal are bounded by 1mm thickness adhesive. The sheet metal was pulled in the opposite direction along each axial axis. This is also called shear lag model, first published by O. Volkersen [18]. Differently as normal contact problems, out-of-plane normal stress are ignored in shear lag model analysis [92]. Shear stress distribution along the adhesive layer will be studied in this section. The results will be compared with the theoretical value and the simulation value.

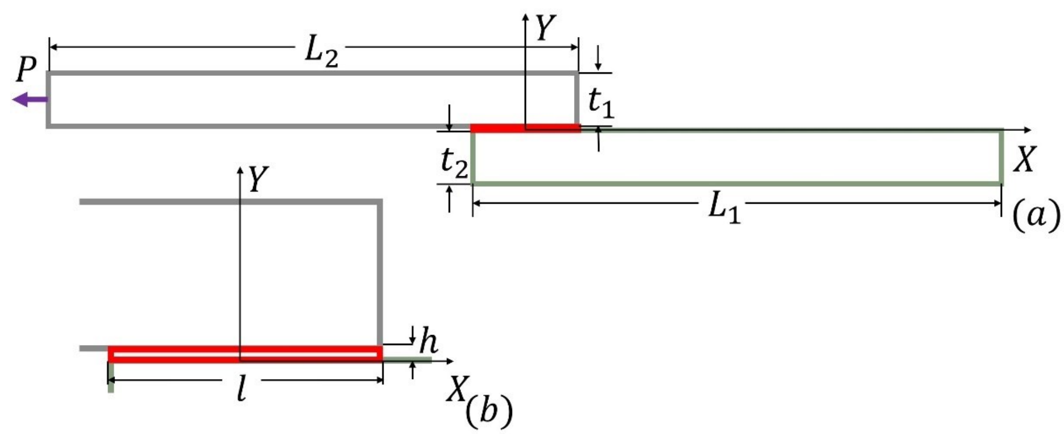

Figure 21. (a) Schematic for single lap joint, (b) close up at the adherend.

Once the adherends are rigid, the value of shear stress along the adhesive layer is constant. On the other hand, if the adherends are elasticity with a constant elasticity modulus, the shear stress distribution follows [92]:

$$\tau(x) = \frac{Pw}{2\sinh\left(\frac{wl}{2}\right)}\cosh(wx) + \frac{Pw}{2\cosh\left(\frac{wl}{2}\right)}\left(\frac{E_2t_2 - E_1t_1}{E_2t_2 + E_1t_1}\right)\sinh(wx). \tag{22}$$

where $\tau(x)$ is the shear stress, *P* is force per unite width; E_1 and E_2 are the Young's moduli of the adherends; $t_1$and t_2 are the thickness of adherends, *l* is the length of the lap; the expression of the coefficient w is:

$$w = \sqrt{\frac{G}{h}\left(\frac{E_2t_2 + E_1t_1}{E_2t_2E_1t_1}\right)} \tag{23}$$

where *G* is shear modulus of the adhesive; *h* is the thickness of the adhesive layer; the origin of the *x*-axis is the middle point of the lap.

Figure 22. The dimensions of the model are chosen followed: For the adherends, the length $L_1 = L_2 = 50$ mm, the thickness $t_1 = t_2 = 5$ mm, the Young's modulus $E_1 = E_2 = 71$ GPa; for the adhesive, the length of the lap $l = 10$ mm, the thickness $h = 0.1$ mm, the shear modulus $G = 3.85$ GPa. Force *P* = 400 N is applied on the top adherend in the negative *x*-direction.

A 2D plane strain finite element model is built for the simulation and the optimization as shown in

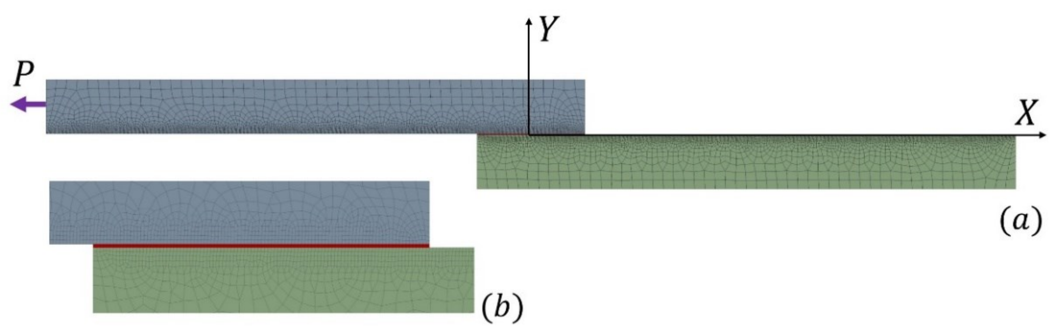

Figure 22. (a) FE mesh for the single lap joint, (b) close up to adhesive.

For the boundary conditions, the bottom adherend is fixed at the right end. The adhesive layer is bounded with the adherend. The bounded region is considered as the contact region. The free region for the measurement in x-direction is picked from the top edge of the bottom adherend. The displacement in x-direction $\bar{u}_i$ and u_i are fed into the proposed method. Finer meshes around the CR and FR are used to keep the accuracy of the simulation. Coarse mesh on the other area makes the program more efficient.

To apply the shear stress, CR is refined into 10 segments with the same size as shown in Figure 23. The x-displacement $\bar{u}_i$ of the 10 points along the FR are fed into the proposed numerical scheme.

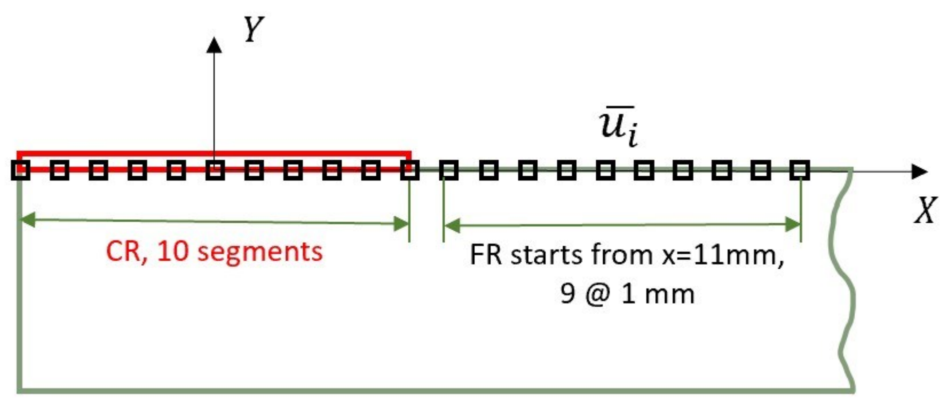

Figure 23. Discretization of contact and free regions

8.2 Result and Algorithm Evolution

The theoretical shear stress distribution is calculated by Eqn. (22). Due to the limitation of the ANSYS Workbench, which doesn't have the function to apply the piecewise linear shear pressure along a surface, the step load function, Eqn. (2) is employed in this chapter. Based on the differential shear phenomenon, maximum shear stress occurs on the two edges of the lap and the minimum shear stress occurs at the middle of the lap [93]. Therefore, a constraint equation, can be generated as:

$$\begin{cases} P_{i+1} \geq P_i, & i \leq 5, \\ P_{i+1} \leq P_i, & i > 5. \end{cases} \tag{24}$$

Because CR is refined into 10 segments as Figure 23 depicts, i is an even value in Eqn. (2). The inflexion of the constraint equation, Eqn. (24), can be picked at i = 5 or i =6. To expedite the convergence and achieve a more accurate solution, the optimization program is constrained by Eqn. (12), (15) and (24). Not that the forces in Eqn. (12) in this problem are in the x-direction. Two sets of the results of the average relative error ϵ and the reaction force R solved by Eqn.(11) are listed in Table 6. Note that $\bar{u}_i$ and u_i will be fed into Eqn. (16) instead of $\bar{v}_i$ and v_i. It is readily seen that the effective of Eqn.(12) is not as significantly as the previous examples. The constraint even does not impose the reaction force R to 400 N.

Table 6. Computed average relative error ϵ and reaction force R of single lap joint.

Eqn. (12)included	ϵ (%)	R (N)
No	0.0175	405.49
Yes	0.0163	405.49

The shear stress distribution is posted in Figure 24. The simulation result is slightly different from the theoretical result. For the predicted results under a different constraint condition, it is hard to judge which one is in better agreement with the simulation or the theoretical results. However, the results with the constraint with Eqn. (

12) have more accurate maximum shear stress. The unwilling results might be caused by the fact that the peeling stress is not considered during the analysis. As elaborated previously, using piecewise linear function to apply the shear pressure might increase the accuracy as well. To a certain extent, the results still can present the shear stress distribution.

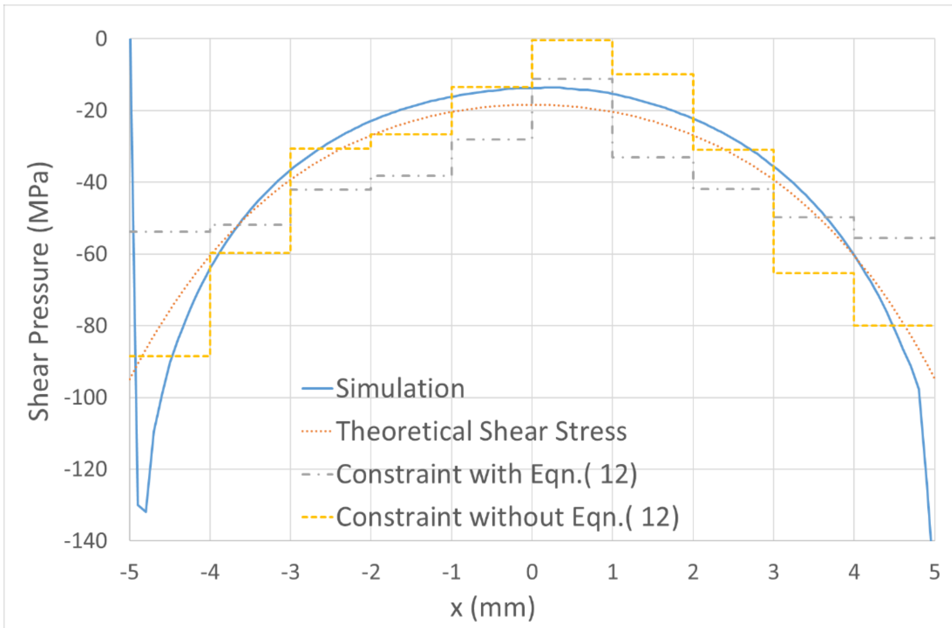

Figure 24. Theoretical and simulated shear stress vs. calculated shear stress for the single lap joint.

CHAPTER NINE

DAMGE IDENTIFICATION

9.1 Problem Description

An insufficient boundary problem is studied in this section as depicted in Figure 25. A rectangular beam is partially hidden. In the hidden area (unobservable area), the beam has a through damage on the top edge. The model represents a practical problem, which relates to damage detection. Further, in this study, the novel hybrid method is used to identify the size and the location of an unobservable damage. Two different shapes, semicircle and isosceles triangle, of damage are studied separately in this chapter.

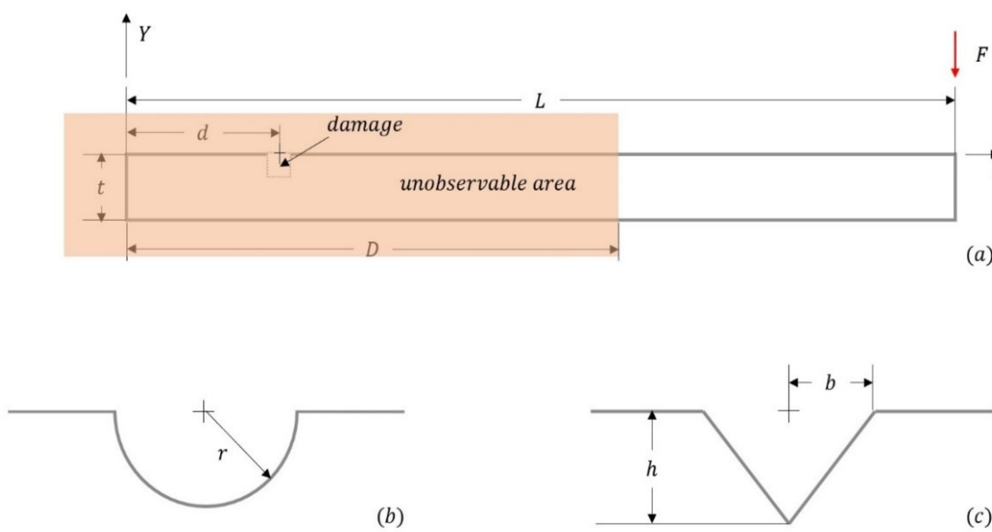

Figure 25. (a) Schematic for a beam with a damage in an unobservable area, (b) semicircle damage, (c) isosceles triangle damage.

A full-size plane stress model is employed for the study. The following geometric parameters are chosen for the problem: length of the beam $L = 500$ mm, the height of the beam $t = 20$ mm, the width of the beam which is the thickness of the model is 20. mm, the length of the unobservable area $D = 320$ mm, the location of the center of the damage $d = 137$ mm, the radius of the semicircle $r = 1.3$ mm, the base of the triangle $b = 1.3$ mm , the height of the triangle $h = 3.3$ mm. Further, the material of the beam is aluminum alloy with the Young's modulus $E = 71$ GPa and Poisson's ratio $v = 0.33$.

The finite element mesh for the beam is shown in Figure 26. For the optimization, the variables setting for each shape are *d* and *r* for the model with semicircle and *d*, *b* and h. for the model with isosceles triangle. The semicircle is meshed into divisions of size of $\frac{\pi r}{50}$, and the triangle is meshed with the element size of 0.1 mm. The edge around the damage has the same mesh size as the damage. The edge that coincides with the *y*-axis is rigidly restrained. A force $F = 50$ N in the negative *y*-direction is applied on the right edge of the beam.

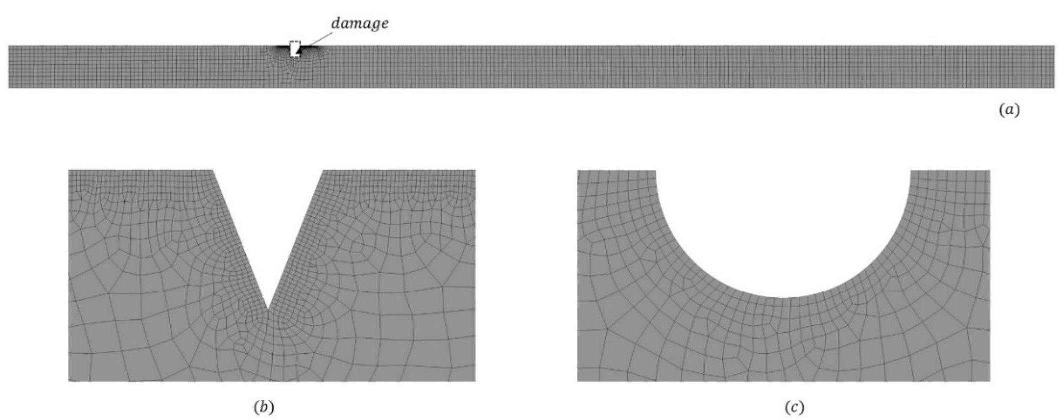

Figure 26. (a) FE mesh for a beam with a damage in an unobservable area, (b) mesh around semicircle damage, (c) mesh around isosceles triangle damage.

Numerically simulated y-displacements at nodes on the edge of the observable beam are used in place of the actual experimental measurement. Because of that the insufficient boundary is a damage, the contact region is not suitable for this problem. However, the free region keeps the same definition and function as that in the previous chapters. FR is defined as starting from $x = 200$. There are ten points selected with the equal space at 20 mm. The y-displacements $\bar{v}_i$ for each point is to be fed into the proposed numerical scheme.

9.2 Result and Algorithm Evolution

The objective of the application of the proposed technique in this chapter is to identify the parameters of a damage on the beam. The size and the location of the damage is given, but they are assumed as unknown in the optimization. There is no other method which is adapted for the results comparison. The optimization results are compared with the real parameters of the damage only.

In this problem the input load F is a constant number. The geometry of the problem is the part that need to be optimized. The stiffness matrix $\mathbf{K}$ is changed to a combination of several matrices which depends on the variables r, d, b and h. Hence, the minimization becomes as follows.

$$\min_{r,d,b,h} \sum_{i=1}^{\alpha} \frac{1}{2} \|\bar{v}_i - \{\mathbf{AK}(r,d,b,h)^{-1}\mathbf{F}\}_i\|^2. \tag{25}$$

Due to the restriction from the geometry of the beam, the damage must be inside the unobservable area of the beam. Further, some constraint equations must be imposed. The constraint equations and the corresponding explanations are listed in Table 7. After some repeated attempts and analysis, it is found that the Nonlinear Programming by

Quadratic Lagrangian (NLPQL) doesn't have a satisfactory performance in this problem. The optimization results are always lost into an inaccurate local solution. This might be caused by that the displacement along the FR is not sensitive enough to the signal from the damage. It might have similar results under different conditions. Numerically, NLPQL is a gradient based algorithm. In a certain precision range, the curve of the Eqn.(25) might not smooth enough for NLPQL to find the solution. Therefore, another powerful global minimization algorithm, Multi-Objective Genetic Algorithm (MOGA), is involved. MOGA is a simple extension of single objective Genetic Algorithm (GA), that GA is a metaheuristic inspired by the process of natural selection that belongs to the larger class of evolutionary algorithms. Genetic algorithms are commonly used to generate high-quality solutions to optimization and search problems by relying on biologically inspired operators such as mutation, crossover and selection [94].

Table 7. Constraint equations and corresponding explanations.

Constraint	Explanations
$d \leq D$	the damage is inside the unobservable area
$r \leq t$	the radius of the semicircle is smaller than the height of the beam
$r \leq d$	prevents the semicircle from penetrating the beam when $d \leq t$
$r \leq D - d$	prevents the semicircle from penetrating the beam when $D - d \leq t$
$b \leq d$	prevents the triangle from penetrating the beam when $d \leq t$
$b \leq D - d$	prevents the triangle from penetrating the beam when $D - d \leq t$
$h \leq t$	the height of the triangle is smaller than the height of the beam

Because the semicircle has only two variables, accurate results can be solved by exhaustion with acceptable iteration steps. The corresponding study is presented in Chapter 4, that is not considered in this chapter. The optimization results by MOGA are shown in Table 8. The predicted characteristic of the damage is close to the true value to a great extent. The application of the proposed method in the damage identification field needs to be integrated in the future so that the program can identify the shape of the damage.

Table 8. Predict size of the damage and the average relative error ϵ.

Semicircle	d (mm)	r (mm)	N/A	ϵ (%)
True value	137	1.3	N/A	N/A
Predict results	137.334	1.301	N/A	0.00092
Isosceles triangle	d (mm)	b (mm)	h (mm)	ϵ (%)
True value	137	1.3	3.3	N/A
Predict results	135.908	1.851	3.265	0.00832

CHAPTER TEN

T-PEEL JOINT

10.1 Problem Description

T-peel joint is a common structure in adhesive and welding manufacturing. Most of the current studies of T-peel joints focus on determination of the strength of the joint by T-peel test. This chapter presents the study of the inverse problem of a T-peel joint employing the proposed novel inverse method. The study includes two sections, the effectiveness of the adhesive dimensions and the stress distribution of the joint.

Figure 27 depicts a sectional view for a T-peel joint. Two specimens bent from thin steel plates into an identical shape are bonded with a layer of adhesive. The following geometric values are chosen. For the specimens, the vertical length $L_{s1} =$ 60 mm, the horizontal length $L_{s2} = 30$ mm. The bent radius $r_c = 2$ mm. The thickness of the specimen is 2 mm. For the adhesive layer, it starts at $s_a = 11.2$ mm. The length $d_a = 15.6$ mm and the thickness $t_a = 1.6$ mm. Further, the Young's moduli for the steel and adhesive are, respectively $E_s = 200$ GPa, $E_a = 40$ GPa, and the Poisson's ratios are $v_s = v_a = 0.3$.

10.2 Effects of Adhesive Dimensions

The first study is about the effect of adhesive dimensions. As Figure 27 depicts, the adhesive layer is defined by three parameters, thickness t_a, starting location s_a, and the length d_a. These three parameters are used as the optimization variables. The inverse method is applied to seek the optimal solution for the variables to match the empirical measurements as close as possible. A two-dimensional plane strain model is built for the simulation and optimization. As Figure 28 depicts, the model is meshed with the element size of 0.2 mm. A 20-N peeling force is applied at the top of the upper specimen. The bottom edge of the lower specimen is fixed rigidly. It is assumed that there is no separation anywhere in the model along the bonding region.

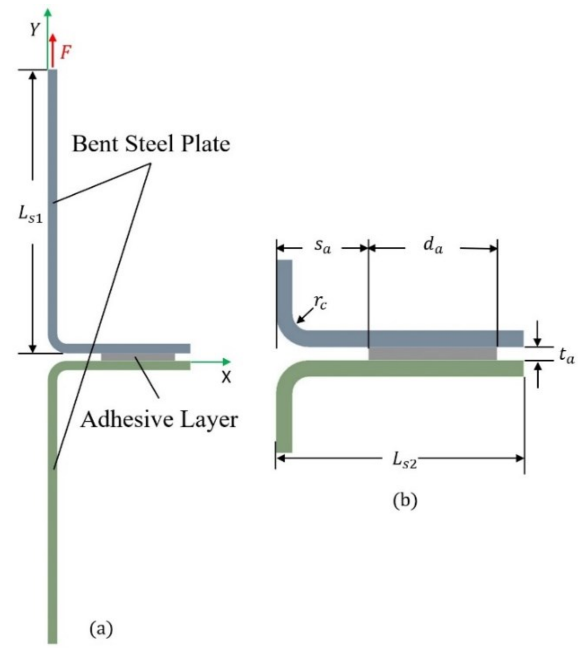

Figure 27. (a) Schematic for T-peel joint, (b) close-up at the adhesive.

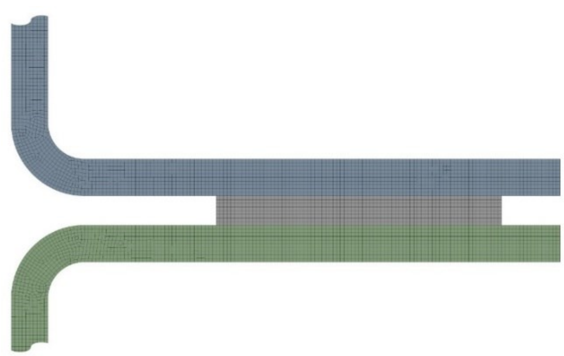

Figure 28. FE mesh for the T-peel joint, close-up at the adhesive.

Similar to the problem in Chapter 9, the stiffness matrix **K** is written as a function of t_a, d_a, and s_a. Therefore, the constrained minimization becomes as follows:

$$\min_{t_a,d_a,s_a} \sum_{i=1}^{\alpha} \frac{1}{2} \| \bar{v}_i - \{\mathbf{AK}(t_a, d_a, s_a)^{-1}\mathbf{F}\}_i \|^2,$$

subject to

$$\begin{cases} t_a > 0 \\ s_a + d_a \leq L_2, \\ s_a \geq \bar{s_a} \end{cases} \tag{26}$$

where α represents the number of the selected nodes for measurement; $\bar{s_a}$ is the minimum value allowed. The constraints imposed on the geometry of the adhesive ensure that the thickness of the adhesive is a positive value, and the adhesive is not longer than the horizontal length of the specimen. The adhesive in the bend area is not considered in this study, so $\bar{s_a} = 4$ mm. In the T-peel test, only the displacements in the *y*-direction are used. The discretization along the free region for the empirical measurements $\bar{v}_i$ is shown in Figure 29. Five equal-spaced points are selected from the horizontal parts and similarly another five points are selected equally from the vertical part. Note that in Figure 29, the selected point $\bar{v}_1$ starts from *x* = 6 mm and $\bar{v}_6$ starts from *y* = 8 mm

The optimization method and process developed in Chapter 9 are utilized here to solve the above constrained minimization problem. The solutions found for the three variables are $d_a = 15.399$ mm, $s_a = 11.397$ mm, $t_a = 0.604$ mm, and the relative error is $\epsilon = 0.013\%$. The relative error is small, although the calculated dimensions of the adhesive are far from the actual data. It is found that when the length of the adhesive d_a exceeds a certain value, it has null effect on the whole structure. As shown in Figure 30, when s_a and t_a are constant and $d_a < 6$ mm, a linear relationship exists between ϵ and

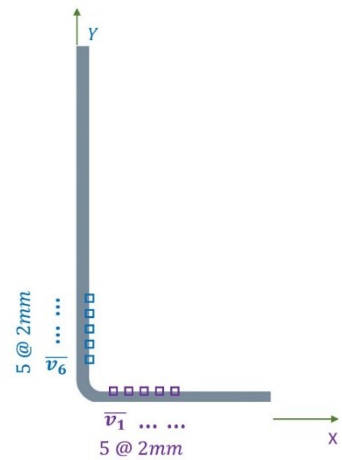

Figure 29. Discretization of free regions for dimensional study.

d_a. However, when $d_a > 6$ mm, the relative error ϵ retains as a constant. And this might be the reason that the solution is not satisfactory. It can be inferred that under the current loading conditions, the real effective length of the adhesive is shorter than the total length d_a. In other words, the adhesive layer might be over designed. Further, a new parameter called limit point, P_l, is introduced to control the value of d_a. It is observed that when d_a exceeds limit point, changes in d_a will no longer affect the value of ϵ.

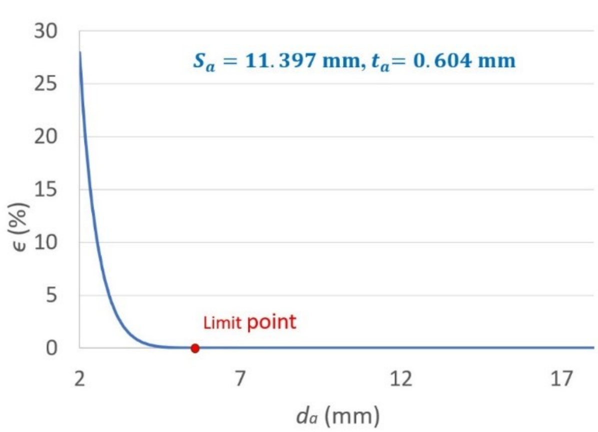

Figure 30. The relationship between the relative error ϵ and the adhesive length d_a.

To validate the above phenomenon, several optimizations under global screening methods with variable control are tested. The issue needs to be classified into two situations, when $d_a \leq P_l$ or $d_a > P_l$. For instance, in Figure 30, the limit point $P_l = 6$ mm. When d_a is smaller than P_l, the optimization program has only one certain solution. This chapter only focuses on the situation when d_a is greater than the limit point. Figure 31 presents the solutions with different specific thickness t_a. The limit point varies based on the change of the thickness and the start point s_a. The relative error ϵ is kept as constant when d_a is over the limit point for all the tests. Hence, the length can be arbitrarily set as the maximum value to reduce the number of variables, that is, $d_a = L_{s2} - s_a$.

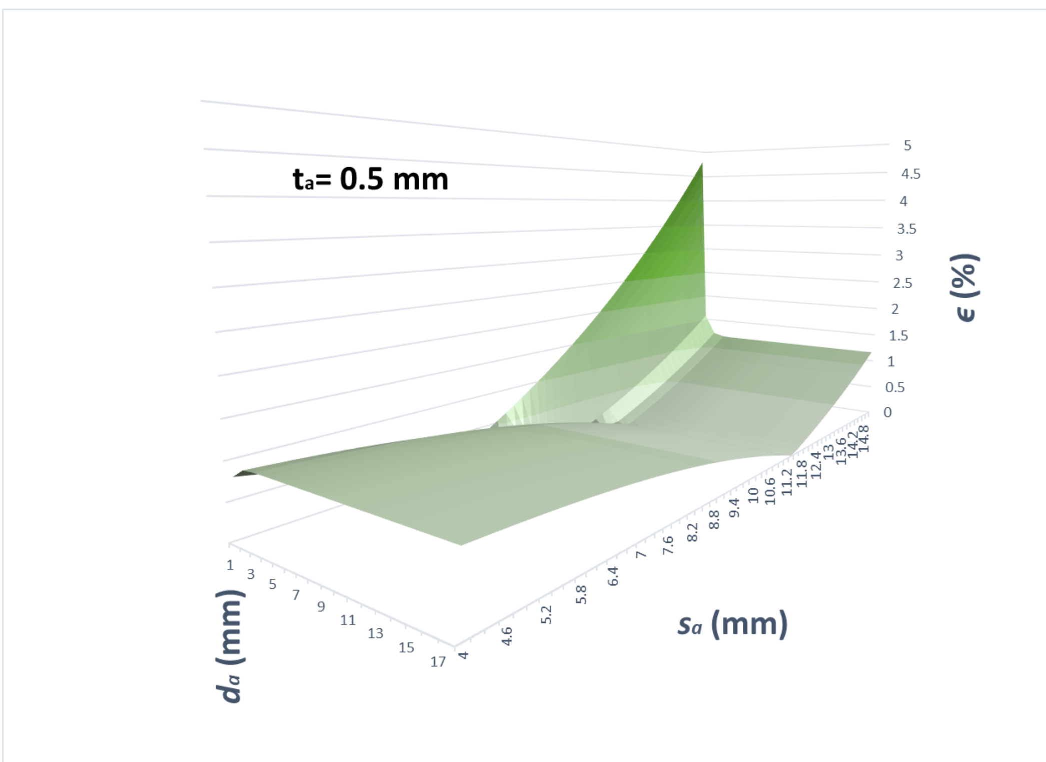

(a)

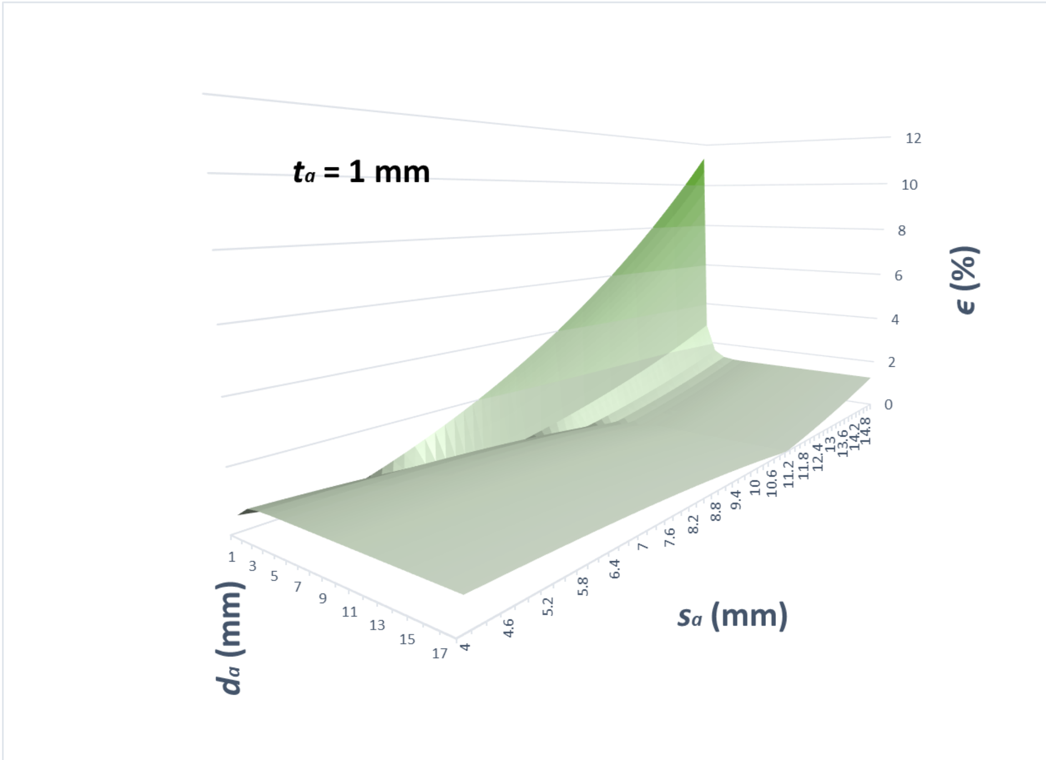

(b)

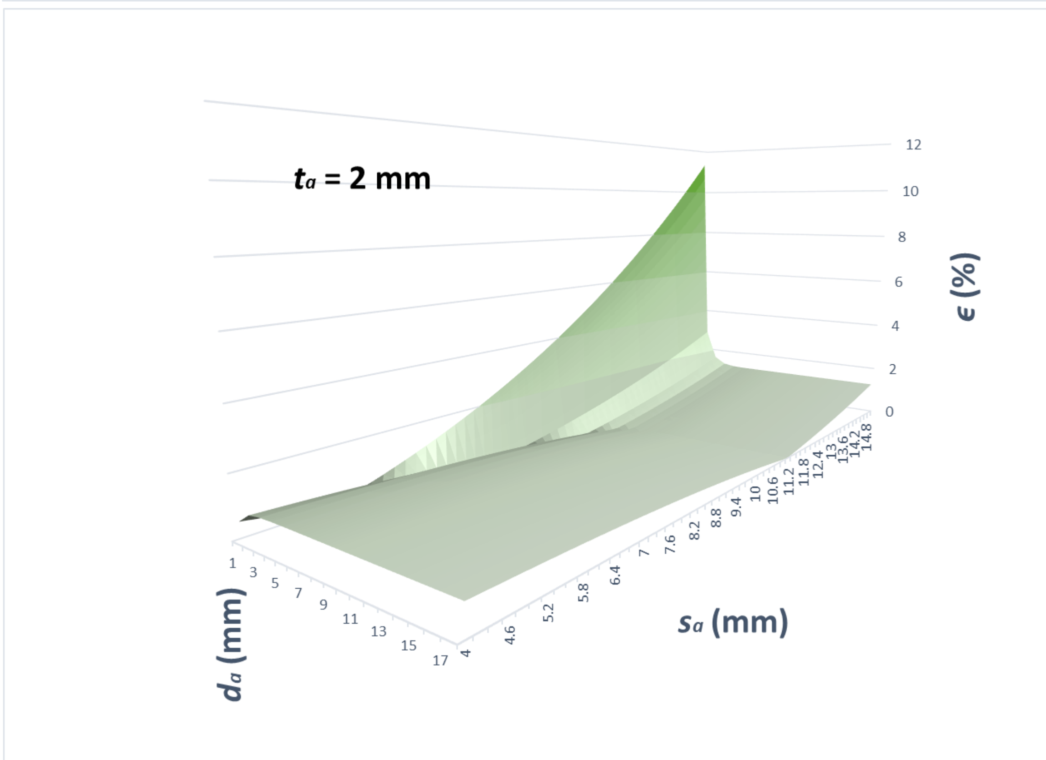

(c)

Figure 31. The correlation of the relative error, the adhesive length, and the starting location when (a) $t_a = 0.5$ mm, (b) $t_a = 1$ mm, (c) $t_a = 2$ mm.

Further the solutions are plotted in Figure 32, the minimum relative error $\epsilon = 0$ is located at $s_a = 11.2$ mm and $t_a = 1.6$ mm, which matches perfectly with the actual value. To check the limit point, Figure 33 presents the stress distribution along the bonding area for the real model. The normal stress exhibits a wave shape. However, the amplitude of the wave is almost negligible when $x > 19$ mm. The normal stress equal to 0 at $x = 19.7$ mm and $x = 25.6$ mm. The relationship between d_a and ϵ when $s_a = 11.2$ mm and $t_a = 1.6$ mm is similar to that in Figure 30. The limit point is at $d_a = 9.7$ mm, where $x = 20.9$ mm. The limit point is located between the two positions where the normal stress equals 0. So far, the methodology can determine the thickness and starting point of the adhesive layer. It cannot be used to determine the length when the adhesive layer is over the limit point. However, the methodology is able to predict the limit point to avert the over design.

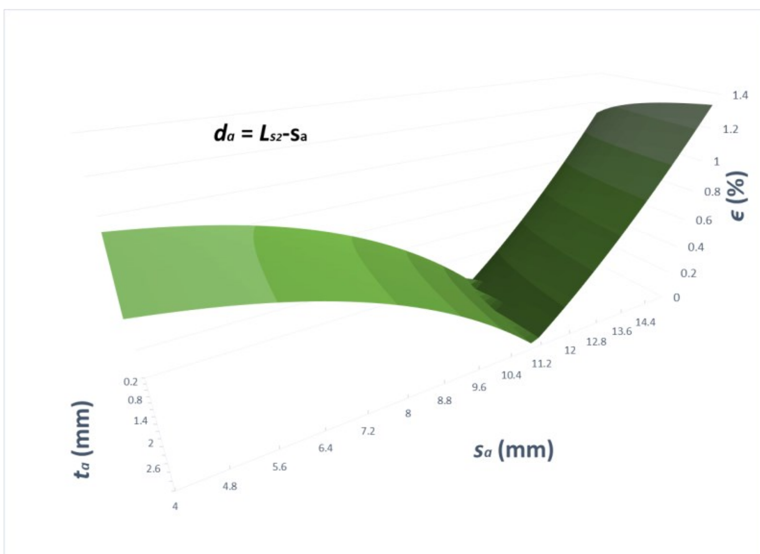

Figure 32. The correlation of the relative error, the starting location, and the adhesive thickness when $d_a = L_{s2} - s_a$.

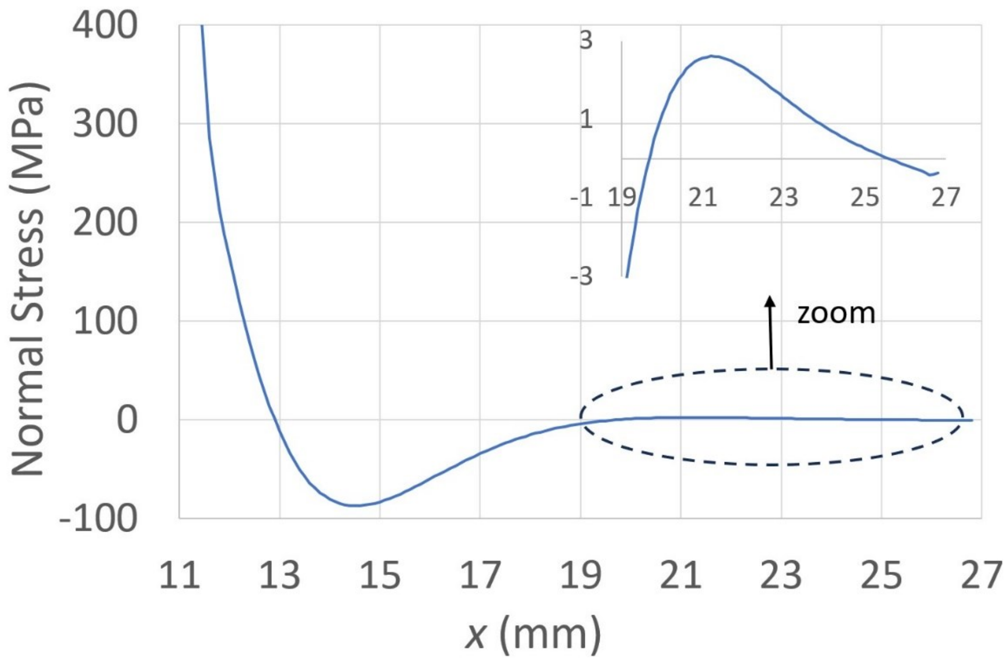

Figure 33. Calculated normal stress distribution along the bonding region.

10.3 Study of Stress Distribution

The geometry of the steel specimen is the same as that in Figure 27. The dimension of the adhesive layer is adjusted to $s_a = 10$ mm, $d_a = 20$ mm and the thickness $t_a = 2$ mm. The finite element mesh remains in the same settings with the mesh size set at 0.2 mm. The boundary conditions and the loading conditions are the same as well. At the early stage of the study, it is found that the bending effect is not negligible. If the bending effect is involved in the proposed method, the amount of the computation will increase exponentially which is prohibited by the hardware resources. Therefore, to eliminate the bending effect, frictionless support is applied on the edges of the specimens that coincide with *y*-axis. This constraint is wildly used in T-peel studies [58].

This study considers only a symmetric model in which only the mesh for the adhesive and the lower specimen, as shown in Figure 34, are included in the following numerical scheme. The measurement points along FR are selected the same way as those in Figure 29, but in the reverse direction. The y-displacements $\bar{v}_i$ for each point is to be fed into the proposed numerical scheme. The bonding region is discretized into different number of divisions to study the effect of the discretization of the bonding region.

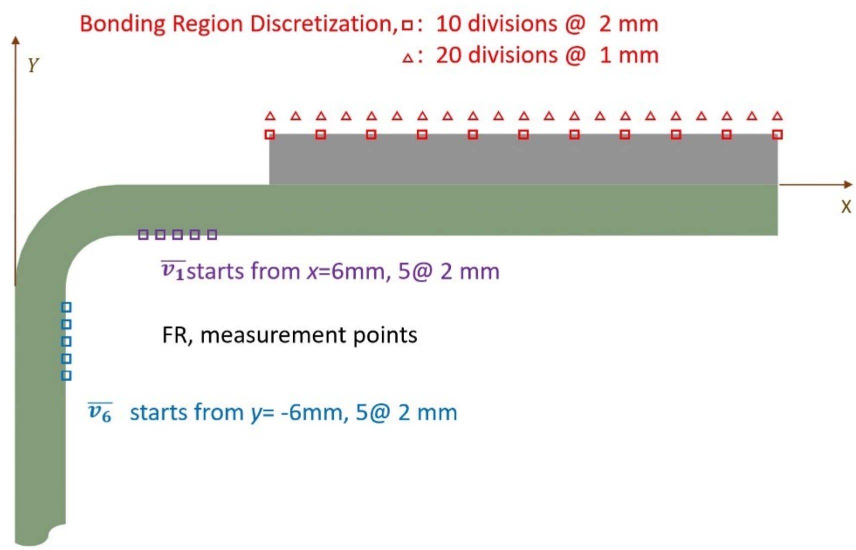

Figure 34. Discretization of bonding and free regions for the study of stress distribution.

For the T-peel joint, a theoretical stress distribution expression does not exist in literature after a thorough search. The most common way to determin the stress disribution along the adhesive relies on using the finite element method. Therefore, only the simulation results, including the normal stress and surface y-displacement, are used as reference for comparison in this section. Further, the piecewise linear loading function is used in this section. Because the normal stress exhibits in the wavy shape as shown in

Figure 33, constraint equations, Eqns. (14), (15) and (17), are not suitable for this problem. To expedite the convergence and achieve a more accurate solution, a new general constraint is imposed on the scheme as follow:

$$\left|\tan^{-1}\left(\frac{p_{i+1}-p_i}{x_{i+1}-x_i}\right)-\tan^{-1}\left(\frac{p_i-p_{i-1}}{x_i-x_{i-1}}\right)\right|\leq\delta. \tag{27}$$

where $\left(\frac{p_{i+1}-p_i}{x_{i+1}-x_i}\right)$ is the gradient of the piecewise linear function, and δ is a controlling parameter arbitrarily chosen to be between 0 to π. The constraint equation is based on the fact that the stress is always distributed continuously and smoothly on elastic materials. When employing piecewise linear functions to approximate a curve function, the discrepancy in gradients between adjacent segments remains minimal provided adequately dense segments are selected. Further, increasing the number of segments results in progressively smaller variations in gradients. On the other hand, once the discretization is determined, the lower the value of δ, the "smoother" the piecewise function. However, the range of the value of δ is defined by the objective mathematical law, dictating the angle between two linear functions lying within the range of 0 to π. When $\delta = 0$ the constraint equation forces the piecewise linear function to behave as one linear function, and $\delta = \pi$ invalidates the constraint equation. In actual mechanical problems, δ usually does not exceed 0.5 π. In this study, δ is set equal to 0.5 and 1.2, with their effects presented later in the study.

Two configurations of discritazation along CR as depicted in Figure 34 are analyzed. For convenience, 10 segments discretization is set in configuration 1, and configuration 2 has 20 divisions. Even though Eqn. (12) is not applied as a constraint, the reaction force at the fixed end still needs to be checked. Computed average relative error ϵ and reaction force R are presented in Table 9. The reaction force for both configurations is almost the same. When $\delta = 1.2$, reaction force R found for configuration 1 is closer to the actual force 20N, but configuration 2 has smaller relative errors.

Table 9. Computed average relative error ϵ, reaction force R of the T-peel joint analysis.

Configuration	δ	ϵ (%)	R (N)
1	0.5	0.397	20.143
1	1.2	0.389	20.149
2	0.5	0.424	20.147
2	1.2	0.304	20.154

Figure 35 depicts the stress distribution along the bonding region. The solution for configurations 1 and 2 might be similar based on the relative error ϵ. However, from Figure 35, predicted normal stress for configuration 2 matches more closely to the simulation stress. The main differences are concentrated at $0 \leq x \leq 7$ mm, especially for the maximum normal stress at $x = 0$. As presented previously, lower values of δ yield curves of greater smoothness. However, the results from Table 9 contradict with the expectation that smoother curves enhance precision in outcomes. This discrepancy arises due to the inadequate discretization of the bonding surface, which fails to accurately capture the variability within the 2 mm $\leq x \leq$ 6 mm range. It is predicted that with an increase in the fineness of discretization, the adoption of smaller δ values could potentially lead to improvements in accuracy.

At the following stage of the study for the T-peel joint, constraint Eqn. (27) is not considered. The negative normal stress and the wave shape are ignored. The optimization program is under the constraint equations Eqns. (12), (14),   and (17). However, missing negative normal stress did not yield “bad solutions”. As Figure 36 presents, if we only use the relative error ϵ as criteria, the solution has higher accuracy compared to that in Table 9. This issue might be due to the following two sources:

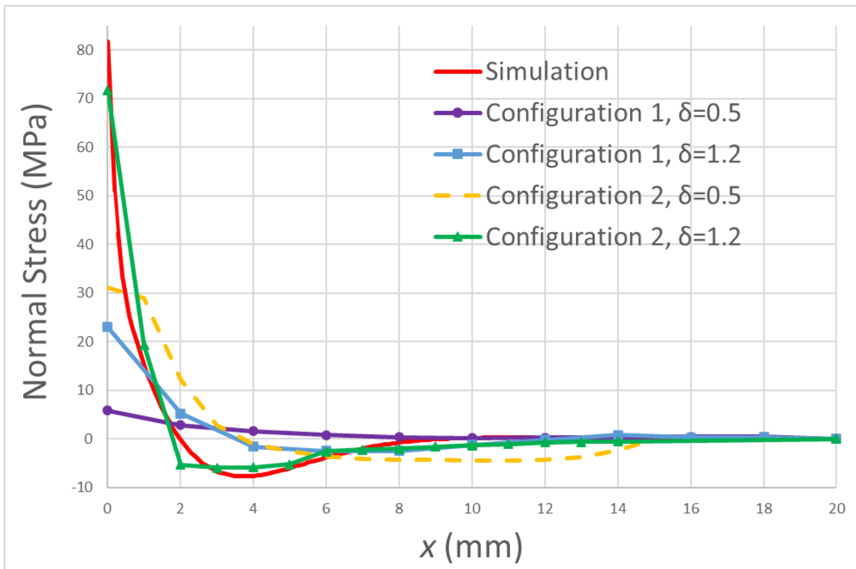

Figure 35. Stress distribution along the bonding region.

1. The reaction force is a vital parameter in the proposed scheme. The improper settings provided the constraint on the reaction force, so it can have better solutions.
2. The larger the value of δ, the more negligible the constraining effect of Eqn. (27) becomes. A “weak” constraint needs more samples and computations. Due to the limitation of the hardware, the solution might not be acceptable.

It can be predicted that with a finer discretization and a smaller value of δ, the results tend to be more accurate. Of course, the computation time increases drastically as well. A study of the effects of constraint Eqn. (27) is presented in Appendix C for reference.

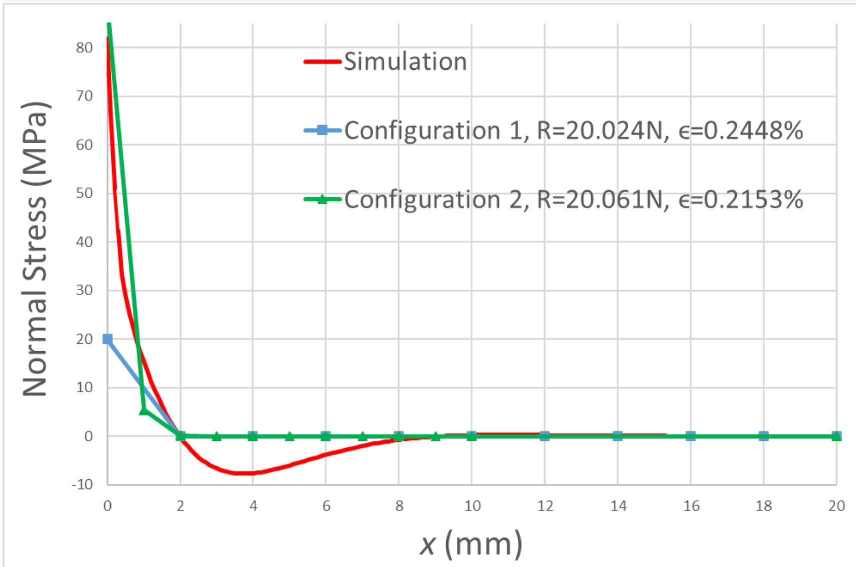

Figure 36. Stress distribution along the bonding region excluding Eqn. *(27).*

CHAPTER ELEVEN

CONCLUSION AND FUTURE WORK

11.1 Conclusion and Key Findings

In the automotive industry, the integration of multiple components through various joining methods is fundamental to vehicle assembly. One of the critical challenges faced in this sector is managing insufficient boundary conditions, particularly the contact stress between components, which significantly impacts the failure rates and lifespan of parts. This dissertation has presented a novel hybrid technique that incorporates empirical measurements into numerical simulations to accurately determine contact pressure and address other insufficient boundary issues. The study about the contact problems in this dissertation has been published in the journal Meccanica [95].

This study utilized simulated displacements at select points on the free surface of the target object as proxies for actual experimental measurements. The proposed numerical scheme is posed as a contained optimization problem in which the error between the known and the calculated displacements is minimized. Seven examples are chosen to demonstrate the accuracy and efficiency of the proposed numerical scheme. The results demonstrated that the calculated contact pressures were consistently in alignment with theoretical expectations or simulated outcomes, underscoring the potential of this methodology. It raises the prospect of developing the proposed methodology into a non-destructive testing (NDT) tool with which the contact pressure between two objects can be determined once the surface displacements are obtained through an optical means.

Constraints were strategically incorporated alongside the error function to enhance the accuracy and computational efficiency of the analysis. The study of the impact of constraint equations on the solution accuracy was conducted. This analysis highlighted the critical role of constraints within the optimization framework, significantly enhancing the model’s reliability and accuracy. Especially, Chapter 10 emphasized the gradient constraint, Eqn. (27) which was pivotal in accurately modeling the stress distribution in adhesive joints during T-peel tests. This specific constraint effectively managed the gradient of the stress field, ensuring that the simulations adhered closely to the physical behavior observed in experimental tests. This precise application of gradient constraints underscores their capacity to refine predictions and guide the optimization process towards solutions that reflect physically realistic outcomes.

11.2 Future Prospects and Challenges

The potential to expand the application of this hybrid technique into other areas of ill-posed problems, such as single lap joints (tangential stress) and damage identification, is evident. However, these applications require further development to realize their full potential. The next phases of research will focus on several critical areas:

- Searching for more robust numerical optimization methods that are adaptive to these specific engineering problems will be essential for enhancing the reliability and versatility of the technique.
- Investigating the sensitivity of the proposed technique to the inherent errors in empirical data will help refine the measurement and calculation processes.
- Currently, the study is based on two-dimensional models. Extending the research to three dimensions is crucial for a deeper understanding of real-world problems.

Developing three-dimensional models will enhance predictive accuracy and applicability, allowing for more comprehensive solutions to intricate engineering challenges.

- Integration works on for the damage identification are necessary to fully develop the damage identification component of this technology, which might revolutionize how industries approach maintenance and safety assessments.
- Expanding the application of this technique to address other insufficient boundary conditions could broadly increase its industrial applicability.

The development of a hybrid finite element method, as discussed in this dissertation, signifies a substantial advancement in the analytical capabilities available to mechanical engineers, particularly in the automotive industry. By combining empirical data with numerical modeling, this research might lay the foundation for more reliable and efficient design and testing methods. As this method evolves, it has the potential to become an indispensable tool in the engineering toolkit, offering precise, efficient, and versatile solutions to complex mechanical problems.

APPENDIX A

THEORY OF CONSTRAINED MINIMIZATION PROBLEM

A.1. Nonlinear Programming by Quadratic Lagrangian

Nonlinear Programming by Quadratic Lagrangian (NLPQL) [87, 88] is a sequential quadratic programming (SQP) method which is an algorithm used for solving constrained nonlinear optimization problems. In the field of real numbers, the problem can be formed as:

$$\min_{x} f(x), \tag{A1}$$

subject to:

$$u_i(x) = 0, i = 1, \dots \dots, m_e$$

$$g_j(x) \leq 0, j = 1, \dots \dots, m_i$$

where $f(x)$ is the objective function, $u_i(x)$ and $g_j(x)$ are, respectively, the equality and inequality constraints.

The Lagrangian for the problem is:

$$\mathcal{L}(x, \lambda, \mu) = f(x) + \sum_{i=1}^{m_e} \lambda_i\, u_i(x) + \sum_{j=1}^{m_i} \mu_i\, g_i(x), \tag{A2}$$

where λ_i and μ_i are the Lagrange multipliers. The standard Newton's method is employed to search for the solution of $\nabla\mathcal{L}(x, \lambda, \mu) = 0$ by iterating the following equation:

$$B_{k+1} = B_k + \frac{y_k y_k^T}{y_k^T s_k} - \frac{B_k s_k s_k^T B_k}{s_k^T B_k s_k}, \tag{A3}$$

where B_k is the Hessian of the Lagrangian, $s_k = x_{k+1} - x_k$, $y_k = \nabla\mathcal{L}(x_{k+1}) - \nabla\mathcal{L}(x_k)$, and ∇ denotes the gradient. At each iteration, SQP solves a quadratic programming subproblem that approximates the nonlinear optimization problem near the current iterate x_k. This subproblem can be formulated as:

$$\min_{x} \frac{1}{2} p^T B_k p + \nabla f(x_k)^T p, \tag{A4}$$

subject to:

$$u_i(x_k) + \nabla u_i(x_k)^T p = 0, i = 1, \dots \dots, m_e$$

$$g_i(x_k) + \nabla g_i(x_k)^T p \leq 0, j = 1, \dots \dots, m_i$$

where p is the step direction. After solving the quadratic programming subproblem, the solution $p_k$is used to update the current estimate of the solution:

$$x_{k+1} = x_k + \alpha_k p_k, \tag{A5}$$

where α_k is a step size. The algorithm iterates through these steps, adjusting x, λ and μ until convergence criteria are met, typically involving the norm of the gradient of the Lagrangian and the feasibility of the constraints. However, Lagrange multipliers method is only suitable for the problems where constraints must be satisfied exactly. The approach can become complex if the number of constraints is large. Hence, the penalty method will be utilized when handling large numbers of constraints. The penalty method is more flexible in application, especially when an approximate solution is acceptable, or when the constraints cannot be easily incorporated directly into the optimization model. To integrate the penalty method, the objective function can be redefined by adding a penalty term for the constraints:

$$\Phi(x, r) = f(x) + \frac{1}{2} r \left(\sum_{i=1}^{m_e} \|\mu_i(x)\|^2 + \sum_{j=1}^{m_i} \|g_i(x)\|^2 \right), \tag{A6}$$

where r is a positive penalty parameter that controls the influence of the constraint violations. Start with an initial guess x_0, Lagrange multipliers λ and μ, and set a penalty parameter r_0. Construct and solve the quadratic programming problem at each iteration, using the penalized model:

$$\min_{x} \frac{1}{2} p^T B_k p + \nabla\Phi(x_k, r_k)^T p, \tag{A7}$$

subject to:

$$u_i(x_k) + \nabla u_i(x_k)^T p = 0, i = 1, \dots \dots, m_e$$

$$g_i(x_k) + \nabla g_i(x_k)^T p \leq 0, j = 1, \dots \dots, m_i$$

A line search is performed to determine the step size α_k that minimizes the penalized objective function along the direction p_k.

A.2. Genetic algorithms

Genetic algorithm (GA) [94] is a computational search and optimization technique inspired by the principles of natural selection and genetics. GA is used to solve complex problems by emulating the process of natural evolution, allowing them to explore large, non-linear, and complex spaces efficiently.

The general process in a genetic algorithm are as follows:

1. Initialization: randomly generate an initial population of individuals, each representing a potential solution to the problem at hand. Each individual is typically encoded as a string of genes, which can be bits, characters, or numbers, depending on the problem.

2. Evaluation: compute the fitness of each individual in the population. This evaluation is based on a fitness function, which is problem specific. The fitness

function plays the role of the environment, ranking individuals according to their ability to exploit or cope with the conditions set by the problem.

3. Selection: select pairs of individuals for reproduction based on their fitness.

4. Crossover and Mutation: apply crossover and mutation operations to create new generations. Crossover is a genetic operator used to vary the programming of chromosomes from one generation to the next. It is analogous to reproduction and biological crossover. Mutation is another genetic operator used to maintain genetic diversity from one generation of a population of genetic algorithm solutions to the next. It is analogous to biological mutation. The classic example of a mutation operator involves a probability that an allele (bit) will be flipped from its original state.

5. Replacement: replace some of or all the population with new individuals.

6. Termination: this process is repeated until some condition is met.

APPENDIX B

PROOF OF UNIQUENESS OF THE SOLUTION

A boundary value problem is illustrated in Figure B1. Where the surface area of the object is $\partial\Omega = \Gamma_1 \cup \Gamma_2 \cup \Gamma_3 \cup \Gamma_4$.

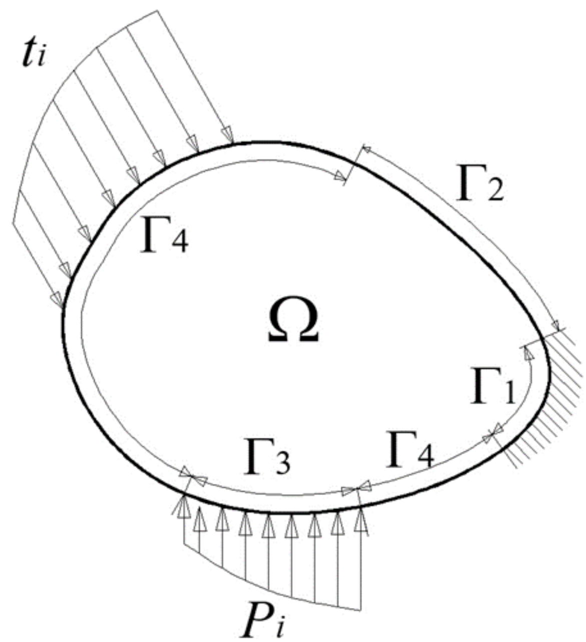

Figure B1. Boundary value problem for proof of uniqueness.

To prove the uniqueness, present the boundary value problem under two different boundary conditions as follows:

Boundary condition I with equation of equilibrium:

$$\sigma_{ij,i} + b_j = 0, \qquad x_i \in \Omega \tag{B1}$$

subject to:

$$u_i = 0, \qquad x_i \in \Gamma_1 \tag{B2}$$

$$\sigma_{ij} n_j = 0, \qquad x_i \in \Gamma_2 \tag{B3}$$

$$\sigma_{ij} n_j = 0, \qquad x_i \in \Gamma_3 \tag{B4}$$

$$\sigma_{ij} n_j = 0, \qquad x_i \in \Gamma_4 \tag{B5}$$

where σ_{ij} is the stress tensor, n_j is the outward normal and b_i is the loading. Note that the equation of equilibrium can be written in terms of the displacement known as Navier's equation.

$$\mu u_{i,jj} + (\lambda + \mu) u_{j,ji} + b_i = 0. \tag{B6}$$

Here, Hook's law for linear elastic material is used.

$$\sigma_{ij} = \lambda \delta_{ij} u_{k,k} + \mu\left(\mu_{i,j} + \mu_{j,i}\right). \tag{B7}$$

where λ and μ are the Lamé constants. Once the problem is solved, the displacement on the surface Γ_2 can be determined as:

$$u_i = f_i(x_i), \qquad x_i \in \Gamma_2 \tag{B8}$$

Further, for the boundary condition II. The equilibrium Eqn. (B1) subjects to:

$$u_i = 0, \qquad x_i \in \Gamma_1 \tag{B9}$$

$$u_i = g_i(x_i), \qquad x_i \in \Gamma_2 \tag{B10}$$

$$\sigma_{ij} n_j = q_i, \qquad x_i \in \Gamma_3 \tag{B11}$$

$$\sigma_{ij} n_j = t_i, \qquad x_i \in \Gamma_4 \tag{B12}$$

$$\sigma_{ij} n_j = 0, \qquad x_i \in \Gamma_2 \tag{B13}$$

The geometry and material properties of these two problems are identical. Besides, the loading, b_i and t_i, and the boundary subdivisions Γ_i are also the same for the two problems. Due to the over-specification of the boundary condition (A.13), Problem II becomes ill-posed. Now consider the following theorem.

Theorem: Consider the following well-posed boundary value problem as shown in Figure B2. Involving a linear elastic object occupying volume Ω with the boundary surface area $\partial\Omega = S_1 \cup S_2$.

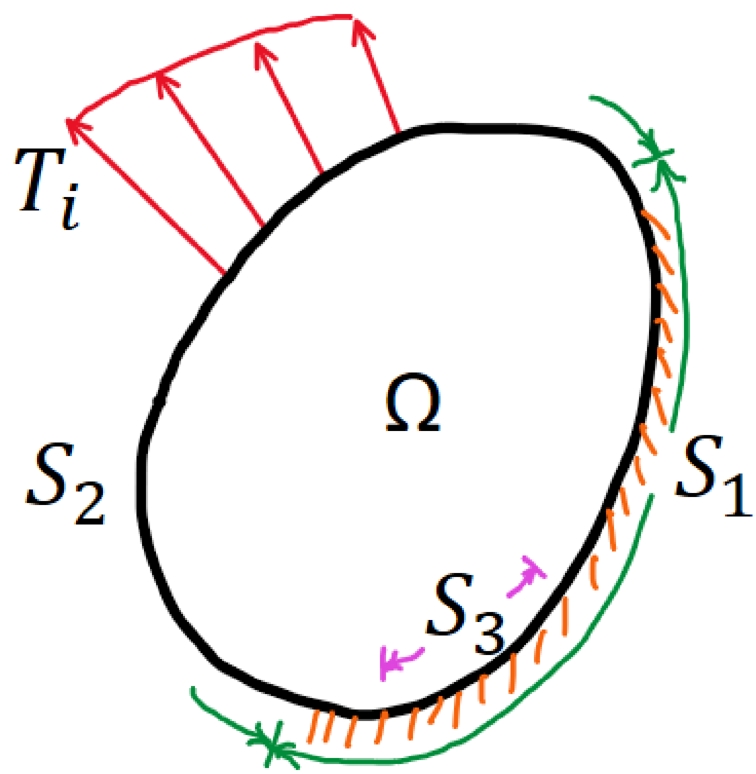

Figure B2. Well-posed boundary value problem

The boundary conditions for this problem are following:

$$\sigma_{ij,i} = 0, \quad x_i \in \Omega, \tag{B14}$$

$$w_i = \bar{w}_i, \quad x_i \in S_1 \neq \emptyset, \tag{B15}$$

$$\sigma_{ij} n_j = T_i, \quad x_i \in S_2, \tag{B16}$$

where w_i is the displacement, $\bar{w}_i$ is the prescribed displacement, and T_i is the surface traction. For an arbitrary set $S_3 \neq \emptyset$, in S_1, $S_3 \subseteq S_1$, if

$$\sigma_{ij} n_j = 0, \quad x_i \in S_3 \subseteq S1, \tag{B17}$$

then we must have

$$T_i = 0.$$

The proof is followed. First, integrate the first boundary condition, $\sigma_{ij,i} = 0$, over the entire volume:

$$\int_{\Omega} \sigma_{ij} d\Omega = 0, \tag{B18}$$

or, after applying the divergence theorem of Gauss,

$$\int_{S} \sigma_{ij} n_j dS = 0. \tag{B19}$$

This can be represented by the following equation of equilibrium in the global sense.

$$\int_{S_1} \sigma_{ij} n_j dS + \int_{S_2} T_i dS = 0. \tag{B20}$$

Next, two cases are discussed. Case 1, when $S_3 = S_1$, Eqn. (B20) becomes, after setting $\sigma_{ij} n_j = 0$ in the first integral,

$$\int_{S_2} T_i dS = 0.$$

For this to hold true over an arbitrary surface area S_2 we must have

$$T_i = 0.$$

Case 2, when $S_3 \subset S_1$. According to the stress-displacement relationship:

$$\sigma_{ij} = \frac{1}{2}(\nabla w_i + \nabla w_i^T)$$

From Eqn. (B15) we have $w_i = 0$. Therefore, σ_{ij}=0 or $\sigma_{ij} n_j = 0$ on boundaryS_1. Eqn. (B20) becomes, after setting $\sigma_{ij} n_j = 0$ in the first integral,

$$\int_{S_2} T_i dS = 0.$$

For this to hold true for an arbitrary S_2 we must have

$$T_i = 0.$$

This completes the proof. The *Theorem* is done.

Now let $u_i$and v_i be the solutions to the boundary values problem under condition I and II, respectively, and w_i be

$$w_i = u_i - v_i.$$

Therefore, the stress defined using w_i is, from Eqn. (B7)

$$\begin{aligned}\sigma_{ij}^w &= \lambda \delta_{ij} w_{k,k} + \mu\left(w_{i,j} + w_{j,i}\right) \\ &= \left[\lambda \delta_{ij} \mu_{k,k} + \mu\left(\mu_{i,j} + \mu_{j,i}\right)\right] - \left[\lambda \delta_{ij} \mu_{k,k} + \mu\left(v_{i,j} + v_{j,i}\right)\right] \\ &= \sigma_{ii}^I + \sigma_{ii}^{II}\end{aligned}$$

Let's examine if σ_{ij} satisfies Eqn. (B14), the equation of equilibrium of the boundary value problem seen in the above theorem.

$$\begin{aligned}\sigma_{ij,i}^w &= (\sigma_{ij}^I - \sigma_{ij}^{II})_{,i} \\ &= (\sigma_{ij,i}^I + b_i) - (\sigma_{ij,i}^{II} + b_i)\end{aligned}$$

Since σ_{ij}^{I} and σ_{ij}^{II} satisfy the equations of equilibrium (B.1) and (B.9), therefore, we have $\sigma_{ij,i}^{w} = 0$. Now consider each boundary condition of boundary conditions I & II, for w_i and its stress σ_{ij}^{w}. First, apparently, on $x_i \in \Gamma_1$, we have

$$w_i = 0$$

On $x_i \in \Gamma_2$, we have

$$w_i = u_i - v_i = f_i - f_i = 0$$

On $x_i \in \Gamma_3$, we have

$$\sigma_{ij}^{w} n_j = (\sigma_{ij}^{I} - \sigma_{ij}^{II}) n_j = p_i - q_i$$

On $x_i \in \Gamma_4$, we have

$$\sigma_{ij}^{w} n_j = \sigma_{ij}^{I} n_j - \sigma_{ij}^{II} n_j = t_i - t_i = 0$$

In summary, the boundary value problem is following:

$$\sigma_{ij,i}^{w} = 0, \quad x_i \in \Omega, \tag{B21}$$

$$w_i = 0, \quad x_i \in \Gamma_1 \cup \Gamma_2, \tag{B22}$$

$$\sigma_{ij}^{w} n_j = p_i - q_i, \quad x_i \in \Gamma_3, \tag{B23}$$

$$\sigma_{ij}^{w} n_j = 0, \ \ x_i \in \Gamma_4. \tag{B24}$$

Further, on $x_i \in \Gamma_2$.

$$\sigma_{ij,i}^{w} = (\sigma_{ij,i}^{I} + b_i) - (\sigma_{ij,i}^{II} + b_i) = 0, \tag{B25}$$

where Eqn. (B3) and (B13) have been used. If we set $S_1 = \Gamma_1 \cup \Gamma_2$, $S_2 = \Gamma_3 \cup \Gamma_4$ and let t_i be defined as follows

$$t_i = \begin{cases} p_i - q_i, \ x_i \in \Gamma_3 \\ 0, \qquad\quad x_i \in \Gamma_4 \end{cases}$$

then, the boundary value problem of Eqn. (B21) ~(B24) is the one defined in the theorem. Therefore, according to the theorem and Eqn. (B25) we must have

$$p_i - q_i = 0$$

From this, we conclude that if the solution to the ill-posed problem under condition II exists, it must be the one that satisfies the problem under condition I. In other words,

$$u_i = v_i$$

and

$$\sigma_{ij}^{I} = \sigma_{ij}^{II}$$

APPENDIX C

STUDY OF GRADIENT CONSTRAINT

The effect of the gradient constraint, Eqn. (27), is studied in block contact problem (Chapter 5) and Hertzian contact problem (Chapter 7). The piecewise linear function is used as loading function. A new configuration 3 for the discretization along the contact region is utilized. Configuration 3 is that the contact region is discretized in to 20 segments with the same size. For the rigid block contact problem, Eqns. (12) and (15) are employed as constraints. Eqn (14) is utilized only for the setting named Ref as reference which is not evolved with Eqn. (27). The corresponding results are listed in Table C1 and Figure C1.

Table C1. Results of block contact problem with gradient constraint

Method	δ	ϵ (%)	R (N)
Ref	N/A	0.07	400.0136
Piecewise Linear	1.2	0.06	401.8564
Piecewise Linear	0.5	7.13	401.9668
Configuration 3	1.2	0.05	400.1690
Configuration 3	0.5	0.04	399.8534

As presented in Chapter 10, when the number of discrete segments is 10 and $\delta = 0.5$, the error in the calculated results is much greater compared to when $\delta = 1.2$. When the sample size is doubled, the results of the two calculations are close, with the accuracy at $\delta = 0.5$ slightly higher than at $\delta = 1.2$. In Figure C1, the contact pressure of the two almost overlap.

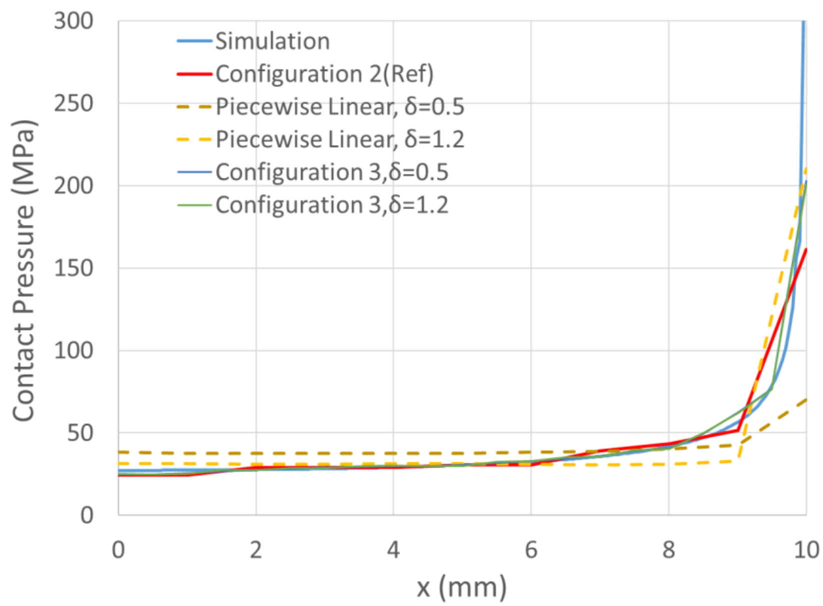

Figure C1. Contact pressure for block contact problem with gradient constraint.

For the Hertzian contact problem, the contact region is set as unknown. Eqns. (12) and (15) are employed as constraints. Eqn. (17) is utilized only for the setting named Configuration 2 (Ref) as reference which is not evolved with Eqn. (27). The corresponding results are listed in Table C2 and Figure C2.

From the results of the Hertzian contact problem, the constraint Eqn. (27) leads to more accurate results. As previously discussed, smaller δ values under finer discretization contribute to more accurate results.

Table C2. Results of Hertzian contact problem with gradient constraint.

Method	δ	ϵ (%)	R (N)	a (mm)
Simulation	N/A	N/A	400	9.857
Configuration 2 (Ref)	N/A	0.0309	400.41	9.556
Configuration 2	1.2	0.0172	400.97	9.551
Configuration 2	0.5	0.0104	401.08	9.586
Configuration 3	1.2	0.0213	400.49	9.670
Configuration 3	0.5	0.0082	400.86	9.579

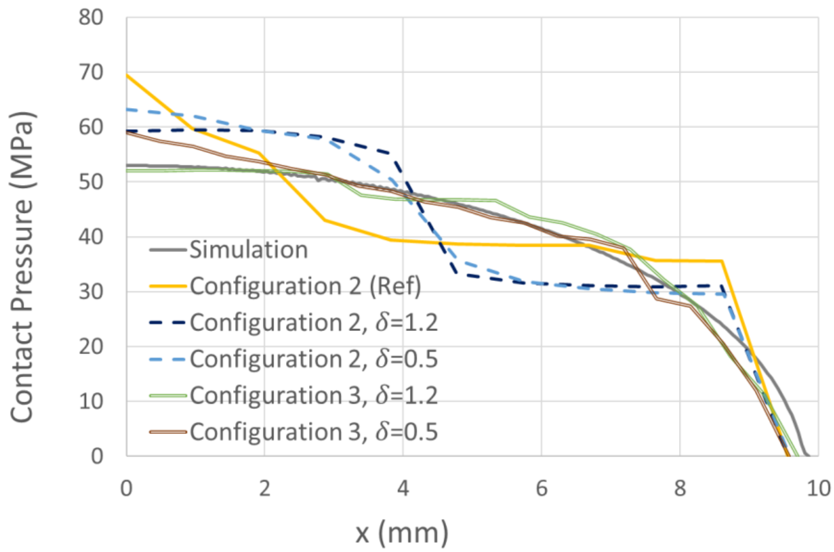

Figure C2. Contact pressure for Hertzian contact problem with gradient constraint.

REFERENCES

1. ANSYS Theory Reference, Release 2023 R1, ANSYS Inc., Canonsburg, PA, (2023).

2. Hertz, Heinrich. “Ueber Die Berührung Fester Elastischer Körper.” *Journal Für Die Reine Und Angewandte Mathematik,* Band 92, December 31, 1882, 156–71. https://doi.org/10.1515/9783112342404-004.

3. Boussinesq, Joseph. *Application des potentiels à l'étude de l'équilibre et du mouvement des solides élastiques*. France: Gauthier-Villars, 1885.

4. Popov, Valentin L., Markus Heß, and Emanuel Willert. *Handbook of Contact Mechanics.* Springer Berlin, Heidelberg, 2019. https://doi.org/10.1007/978-3-662-58709-6.

5. Cook, R.D., D.S Malkus, and M.E. Plesha. *Concept and Applications of Finite Element Analysis*. 3rd ed., Wiley, New York, 1989.

6. Gu, Randy J., P. Murty, and Q. Zheng, “Use of penalty variable in finite element analysis of contacting objects”. *Comput. Struct*, 80 (2002), pp. 2449–2459. https://doi.org/10.1016/S0045-7949(02)00330-9.

7. Campos, L.T., J.T. Oden, and N. Kikuchi, “A numerical analysis of a class of contact problems with friction in elastostatics”. *Comput. Meth*, Appl. Mech. Eng. 34 (1982), pp. 821–845. https://doi.org/10.1016/0045-7825(82)90090-1.

8. Oden, J.T. and N. Kikuchi, “Finite element methods for constrained problems in elasticity”. *Int. J. Numer. Methods Eng*, 18 (1982), pp. 701–725. https://doi.org/10.1002/nme.1620180507.

9. Yagawa, Genki and H. Hirayama. “A finite element method for contact problems related to fracture mechanics.” *International Journal for Numerical Methods in Engineering* 20 (1984): 2175-2195.

10. Chen, Wen-Hwa and P. Tsai, “Finite element analysis of elastodynamic sliding contact problems with friction”. *Comput. Struct*, 22 (1989), pp. 925–938. https://doi.org/10.1016/0045-7949(86)90153-7.

11. Bathe, Klaus-Jurgen and A. Chaudhary, “A solution method for planar and axisymmetric contact problems”. *Int. J. Numer. Methods Eng*, 21 (1985), pp. 65–88. https://doi.org/10.1002/nme.1620210107.

12. Gu, Randy J.. “Moving finite element analysis for two-dimensional frictionless contact problems.” *Computers & Structures* 33 (1989): 543-549. https://doi.org/10.1016/0045-7949(89)90028-X.

13. Fuehne, Joseph P. and Johan Engblom. “Finite Element/Penalty Function Method for Computing Stresses near Debonds.” *AIAA Journal* 30 (1992): 1625-1631. https://doi.org/10.2514/3.11110.

14. El-Abbasi, Nagi and K.J. Bathe, “Stability and patch test performance of contact discretizations and a new solution algorithm”. *Comput. Struct*, 79 (2001), pp. 1473–1486. https://doi.org/10.1016/S0045-7949(01)00048-7.

15. Maniatty, Antoinette, Nicholas Zabaras, and Kim Stelson. “Finite Element Analysis of Some Inverse Elasticity Problems.” *Journal of Engineering Mechanics* 115, no. 6 (June 1989): 1303–17. https://doi.org/10.1061/(asce)0733-9399(1989)115:6(1303).

16. Adams, Robert D., and William C. Wake. *Structural Adhesive Joints in Engineering*. 1984. https://doi.org/10.1007/978-94-009-5616-2.

17. Silva, Lucas F.M. da, Paulo J.C. das Neves, R.D. Adams, and J.K. Spelt. “Analytical Models of Adhesively Bonded Joints—Part I: Literature Survey.” *International Journal of Adhesion and Adhesives* 29, no. 3 (April 2009): 319–30. https://doi.org/10.1016/j.ijadhadh.2008.06.005.

18. Volkersen, O. "Die Niektraftverteilung in Zugbeanspruchten mit Konstanten." *Laschenquerschnitten Luftfahrtforschung,* 15, No. 1, 1938.

19. Ojalvo, I. U., and H. L. Eidinoff. “Bond Thickness Effects Upon Stresses in Single Lap Adhesive Joints.” *SAE Technical Paper Series*, February 1, 1977. https://doi.org/10.4271/770090.

20. DeVries, K. L., M. L. Williams, and M. D. Chang. “Adhesive Fracture of a Lap Shear Joint.” *Experimental Mechanics* 14, no. 3, March 1974: 89–97. https://doi.org/10.1007/bf02324771.

21. Saito, H., and H. Tani. “Vibrations of Bonded Beams with a Single Lap Adhesive Joint.” *Journal of Sound and Vibration* 92, no. 2 (January 1984): 299–309. https://doi.org/10.1016/0022-460x(84)90563-7.

22. Sawa, Toshiyuki, Jiemin Liu, Katsuyuki Nakano, and Junnya Tanaka. “A Two-Dimensional Stress Analysis of Single-Lap Adhesive Joints of Dissimilar Adherends Subjected to Tensile Loads.” *Journal of Adhesion Science and Technology* 14, no. 1 (January 2000): 43–66. https://doi.org/10.1163/156856100742104.

23. Zhao, Bo, Zhen-Hua Lu, and Yi-Ning Lu. “Two-Dimensional Analytical Solution of Elastic Stresses for Balanced Single-Lap Joints—Variational Method.” *International Journal of Adhesion and Adhesives* 49 (March 2014): 115–26. https://doi.org/10.1016/j.ijadhadh.2013.12.026.

24. Azari, S., A. Ameli, M. Papini, and J.K. Spelt. “Analysis and Design of Adhesively Bonded Joints for Fatigue and Fracture Loading: A Fracture-Mechanics Approach.” *Journal of Adhesion Science and Technology* 27, no. 15 (August 2013): 1681–1711. https://doi.org/10.1080/01694243.2012.748434.

25. Ramalho, L. D. C., R. D. S. G. Campilho, and J. Belinha. “Predicting Single-Lap Joint Strength Using the Natural Neighbour Radial Point Interpolation Method.” *Journal of the Brazilian Society of Mechanical Sciences and Engineering* 41, no. 9 (August 13, 2019). https://doi.org/10.1007/s40430-019-1862-0.

26. Dobrzański, Przemysław, and Witold Oleksiak. “Design and Analysis Methods for Composite Bonded Joints.” *Transactions on Aerospace Research* 2021, no. 1 (March 1, 2021): 45–63. https://doi.org/10.2478/tar-2021-0004.

27. Miri, M., M. R. Ayatollahi, A. Akhavan-Safar, and L. F. M. da Silva. “Impact Strength Improvement of Adhesively Bonded Structures Using Natural Date Palm Tree Fibers.” *Mechanics of Advanced Materials and Structures*, December 23, 2022, 1–11. https://doi.org/10.1080/15376494.2022.2158506.

28. Srilakshmi, Rayasam. “Numerical Analysis of Single Riveted Lap Joint Panels Under Tension Load.” *SSRN Electronic Journal*, 2022. https://doi.org/10.2139/ssrn.4297720.

29. Reis, P. NB, J. A. M. Ferreira, and F. Antunes. "Effect of adherend's rigidity on the shear strength of single lap adhesive joints." *International Journal of Adhesion and Adhesives* 31, no. 4 (2011): 193-201. https://doi.org/10.1016/j.ijadhadh.2010.12.003

30. Hu, Bo, Yuan Li, Yu-Tian Jiang, and Huai-Zhong Tang. “Bond Behavior of Hybrid FRP-to-Steel Joints.” *Composite Structures* 237 (April 2020): 111936. https://doi.org/10.1016/j.compstruct.2020.111936.

31. He, Xiaocong. “A Review of Finite Element Analysis of Adhesively Bonded Joints.” *International Journal of Adhesion and Adhesives* 31, no. 4 (June 2011): 248–64. https://doi.org/10.1016/j.ijadhadh.2011.01.006.

32. Douglas, Jesse. “Solution of the Inverse Problem of the Calculus of Variations.” *Transactions of the American Mathematical Society* 50, no. 1 (1941): 71–128. https://doi.org/10.1090/s0002-9947-1941-0004740-5.

33. Nocedal, Jorge, and Stephen J. Wright, eds. "Numerical Optimization." *Springer Series in Operations Research and Financial Engineering*, 1999. https://doi.org/10.1007/b98874.

34. Ravindran, A., K. M. Ragsdell, and G. V. Reklaitis. *Engineering Optimization*. May 2, 2006. https://doi.org/10.1002/9780470117811.

35. Vito, Ernesto De, Lorenzo Rosasco, Andrea Caponnetto, Umberto De Giovannini, and Francesca Odone. "Learning from examples as an inverse problem." *Journal of Machine Learning Research* 6. May (2005): 883-904.

36. Martins, J.M.P., A. Andrade-Campos, and S. Thuillier. "Comparison of Inverse Identification Strategies for Constitutive Mechanical Models Using Full-Field Measurements." *International Journal of Mechanical Sciences* 145 (September 2018): 330–45. https://doi.org/10.1016/j.ijmecsci.2018.07.013.

37. Cooreman, S., D. Lecompte, H. Sol, J. Vantomme, and D. Debruyne. "Identification of Mechanical Material Behavior Through Inverse Modeling and DIC." *Experimental Mechanics* 48, no. 4 (November 22, 2007): 421–33. https://doi.org/10.1007/s11340-007-9094-0.

38. Kang, Y.L., X.H. Lin, and Q.H. Qin. "Inverse/Genetic Method and Its Application in Identification of Mechanical Parameters of Interface in Composite." *Composite Structures* 66, no. 1–4 (October 2004): 449–58. https://doi.org/10.1016/j.compstruct.2004.04.067.

39. Joseph, K. T. "Inverse Eigenvalue Problem in Structural Design." *AIAA Journal* 30, no. 12 (December 1992): 2890–96. https://doi.org/10.2514/3.11634.

40. Olsson, P., and P. Lidström. "Inverse Structural Modification Using Constraints." *Journal of Sound and Vibration* 303, no. 3–5 (June 2007): 767–79. https://doi.org/10.1016/j.jsv.2007.02.003.

41. Sun, Xingsheng, Jie Liu, Xu Han, Chao Jiang, and Rui Chen. "A New Improved Regularization Method for Dynamic Load Identification." *Inverse Problems in Science and Engineering* 22, no. 7 (November 1, 2013): 1062–76. https://doi.org/10.1080/17415977.2013.854353.

42. Wang, Lei, and Xiaojun Wang. "Dynamic Loads Identification in Presence of Unknown but Bounded Measurement Errors." *Inverse Problems in Science and Engineering* 23, no. 8 (January 7, 2015): 1313–41. https://doi.org/10.1080/17415977.2014.993979.

43. Song, Jiangtao, and Randy J. Gu. "A Finite Element-Based Methodology for Inverse Problem of Determining Contact Forces Using Measured Displacements." *Inverse*

Problems in Science and Engineering 20, no. 6 (December 8, 2011): 769–83. https://doi.org/10.1080/17415977.2011.639454.

44. Svec, Otto J. "The Unbonded Contact Problem of a Plate on the Elastic Half Space." *Computer Methods in Applied Mechanics and Engineering* 3, no. 1 (January 1974): 105–13. https://doi.org/10.1016/0045-7825(74)90044-9.

45. Lin, Q., C. Sun, and J. Chen. "Experimental Characterization of Frictional Line Contact by Digital Image Correlation and Inverse Method." *Journal of Engineering Mechanics* 147, no. 11 (November 2021). https://doi.org/10.1061/(asce)em.1943-7889.0002007.

46. Doebling, S W, Farrar, C R, Prime, M B, and Shevitz, D W. *Damage identification and health monitoring of structural and mechanical systems from changes in their vibration characteristics: A literature review*. United States: N. p., 1996. Web. https://doi.org/10.2172/249299.

47. Wei Fan, and Pizhong Qiao. "Vibration-Based Damage Identification Methods: A Review and Comparative Study." *Structural Health Monitoring* 10, no. 1 (April 20, 2010): 83–111. https://doi.org/10.1177/1475921710365419.

48. KIM, J.-T., and N. STUBBS. "Improved Damage Identification Method Based on Modal Information." *Journal of Sound and Vibration* 252, no. 2 (April 2002): 223–38. https://doi.org/10.1006/jsvi.2001.3749.

49. Colombo, L., C. Sbarufatti, and M. Giglio. "Definition of a Load Adaptive Baseline by Inverse Finite Element Method for Structural Damage Identification." *Mechanical Systems and Signal Processing* 120 (April 2019): 584–607. https://doi.org/10.1016/j.ymssp.2018.10.041.

50. Li, Mengying, Ziyan Wu, Haifeng Yang, and He Huang. "Direct Damage Index Based on Inverse Finite Element Method for Structural Damage Identification." *Ocean Engineering* 221 (February 2021): 108545. https://doi.org/10.1016/j.oceaneng.2020.108545.

51. Perera, Ricardo, Sheng-En Fang, and Antonio Ruiz. "Application of Particle Swarm Optimization and Genetic Algorithms to Multiobjective Damage Identification Inverse Problems with Modelling Errors." *Meccanica* 45, no. 5 (November 11, 2009): 723–34. https://doi.org/10.1007/s11012-009-9264-5.

52. Li, Tengteng, Maosen Cao, Jianle Li, Lei Yang, Hao Xu, and Zhanjun Wu. "Structural Damage Identification Based on Integrated Utilization of Inverse Finite Element Method and Pseudo-Excitation Approach." Sensors 21, no. 2 (January 16, 2021): 606. https://doi.org/10.3390/s21020606.

53. Friswell, Michael I. "Damage Identification using Inverse Methods." *Dynamic Methods for Damage Detection in Structures,* edited by Michael I. Friswell, CISM International Centre for Mechanical Sciences, vol 499. Springer, Vienna. https://doi.org/10.1007/978-3-211-78777-9_2.

54. Grabowska, J., M. Palacz, and M. Krawczuk. "Damage Identification by Wavelet Analysis." *Mechanical Systems and Signal Processing* 22, no. 7 (October 2008): 1623–35. https://doi.org/10.1016/j.ymssp.2008.01.003.

55. Dessi, Daniele, and Gabriele Camerlengo. "Damage Identification Techniques via Modal Curvature Analysis: Overview and Comparison." *Mechanical Systems and Signal Processing* 52–53 (February 2015): 181–205. https://doi.org/10.1016/j.ymssp.2014.05.031.

56. Dessi, D., and F. Passacantilli. "Damage Identification of 1D and 2D Structures Based on Modal Curvature Analysis." *Developments in the Analysis and Design of Marine Structures*, November 30, 2021, 547–55. https://doi.org/10.1201/9781003230373-62.

57. ASTM D1876-08, Test Method for Peel Resistance of Adhesives (T-Peel Test), 2024, https://doi.org/10.1520/d1876-08r23.

58. Hinopoulos, George and William R. Broughton. *Evaluation of the T-peel Joint Using Finite Element Analysis*. Centre for Materials Measurement & Technology National Physical Laboratory Teddington, Middlesex TW11 0LW, UK,1999.

59. Ben Khalifa, A., Braiek, S., fradj, A. et al. "Experimental investigation of joints strength obtained by ultrasonic welding and soldering under pure T-peel tests using DIC." *Weld World* 67, 495–511 (2023). https://doi.org/10.1007/s40194-022-01437-8.

60. Hadavinia, H., et al. "A Numerical Analysis of the Elastic-Plastic Peel Test." *Engineering Fracture Mechanics*, vol. 73, no. 16, Nov. 2006, pp. 2324–35. https://doi.org/10.1016/j.engfracmech.2006.04.022.

61. Eitner, Ulrich, and Li Carlos Rendler. "The Mechanical Theory behind the Peel Test." *Energy Procedia*, vol. 55, 2014, pp. 331–35. https://doi.org/10.1016/j.egypro.2014.08.096.

62. Dai, Yanwei, et al. "Pre-Notch and Pre-Crack Size Effects on T-Peel Fracture Behaviors of SAC305 Solder Joints." *Theoretical and Applied Fracture Mechanics*, vol. 131, June 2024, p. 104397. https://doi.org/10.1016/j.tafmec.2024.104397.

63. Pereira, J. P. O., et al. "Adherend Effect on the Peel Strength of a Brittle Adhesive." *Procedia Structural Integrity*, vol. 37, 2022, pp. 722–29. https://doi.org/10.1016/j.prostr.2022.02.002.

64. Panthakkal Abdul Muthalif, Mohammed, and Youngson Choe. "Adhesive and Impact-Peel Strength Improvement of Epoxy Resins Modified with Mono and Diamine Functionalized Elastomers." *Advances in Polymer Technology*, edited by Thomas J. Farmer, vol. 2022, Apr. 2022, pp. 1–9. https://doi.org/10.1155/2022/2309235.

65. Khalid, M. Y., et al. "Effect of Anodizing Process on Inter Laminar Shear Strength of GLARE Composite through T-Peel Test: Experimental and Numerical Approach." *Experimental Techniques*, vol. 45, no. 2, Jan. 2021, pp. 227–35. https://doi.org/10.1007/s40799-020-00433-1.

66. Tagimalek, Hadi, and Masoud Mahmoodi. "Experimental Evaluation of T-Peel Strength on Functionally Graded Al5083 and HDPE Tri-Laminated Composites Fabricated by Colding-Assisted Friction Stir Additive Manufacturing." *Journal of Advanced Joining Processes*, vol. 9, June 2024, p. 100174. https://doi.org/10.1016/j.jajp.2023.100174.

67. Nagy, Peter B. "Ultrasonic Classification of Imperfect Interfaces." *Journal of Nondestructive Evaluation* 11, no. 3–4 (December 1992): 127–39. https://doi.org/10.1007/bf00566404.

68. Margetan, F. J., R. B. Thompson, J. H. Rose, and T. A. Gray. "The Interaction of Ultrasound with Imperfect Interfaces: Experimental Studies of Model Structures." *Journal of Nondestructive Evaluation* 11, no. 3–4 (December 1992): 109–26. https://doi.org/10.1007/bf00566403.

69. Quinn, A.M., B.W. Drinkwater, and R.S. Dwyer-Joyce. "The Measurement of Contact Pressure in Machine Elements Using Ultrasound." *Ultrasonics* 39, no. 7 (April 2002): 495–502. https://doi.org/10.1016/s0041-624x(01)00089-0.

70. Zhou, Debao, and Haopeng Wang. "Design and Evaluation of a Skin-like Sensor with High Stretchability for Contact Pressure Measurement." *Sensors and Actuators A: Physical* 204 (December 2013): 114–21. https://doi.org/10.1016/j.sna.2013.10.002.

71. Someya, Takao, Yusaku Kato, Tsuyoshi Sekitani, Shingo Iba, Yoshiaki Noguchi, Yousuke Murase, Hiroshi Kawaguchi, and Takayasu Sakurai. "Conformable, Flexible, Large-Area Networks of Pressure and Thermal Sensors with Organic Transistor Active Matrixes." *Proceedings of the National Academy of Sciences* 102, no. 35 (August 17, 2005): 12321–25. https://doi.org/10.1073/pnas.0502392102.

72. Hung, Y.Y., HuaiMin Shang, and Lian Xiang Yang "Unified approach for holography and shearography in surface deformation measurement and nondestructive testing," *Optical Engineering* 42(5), (1 May 2003). https://doi.org/10.1117/1.1567263

73. Yang, Lianxiang, Yonghong Wang, and Rongsheng Lu. “Advanced Optical Methods for Whole Field Displacement and Strain Measurement.” *2010 International Symposium on Optomechatronic Technologies*, October 2010. https://doi.org/10.1109/isot.2010.5687394.

74. Yang, Lianxiang and Andreas Ettemeyer "Strain measurement by three-dimensional electronic speckle pattern interferometry: potentials, limitations, and applications," *Optical Engineering* 42(5), (1 May 2003). https://doi.org/10.1117/1.1566781

75. Chen, Fanxiu, Xu Chen, Xin Xie, Xiu Feng, and Lianxiang Yang. “Full-Field 3D Measurement Using Multi-Camera Digital Image Correlation System.” *Optics and Lasers in Engineering* 51, no. 9 (September 2013): 1044–52. https://doi.org/10.1016/j.optlaseng.2013.03.001.

76. Reddy, J. N. *Introduction to the Finite Element Method*. McGraw Hill Education, 2019.

77. Moaveni, Saeed. *Finite Element Analysis: Theory and Application with Ansys*. S.l.: Prentice Hall, 2020.

78. Kreyszig, E. *Advanced Engineering Mathematics*. New York: John Wiley & Sons, 2006.

79. Ravindran, A., G. V. Reklaitis, and K. M. Ragsdell. *Engineering Optimization: Methods and Applications*. Hoboken, NJ: John Wiley & Sons, 2006.

80. Chapra, Steven C., and Raymond P. Canale. *Numerical Methods for Engineers*. New York, NY: McGraw-Hill, 2021.

81. Branch, Mary Ann, Thomas F. Coleman, and Yuying Li. “A Subspace, Interior, and Conjugate Gradient Method for Large-Scale Bound-Constrained Minimization Problems.” *SIAM Journal on Scientific Computing* 21, no. 1 (January 1999): 1–23. https://doi.org/10.1137/s1064827595289108.

82. Levitin, E.S., and B.T. Polyak. “Constrained Minimization Methods.” *USSR Computational Mathematics and Mathematical Physics* 6, no. 5 (January 1966): 1–50. https://doi.org/10.1016/0041-5553(66)90114-5.

83. Blanchard, Philippe, and Erwin Brüning. “Constrained Minimization Problems (Method of Lagrange Multipliers).” *Mathematical Methods in Physics*, 2003, 403–11. https://doi.org/10.1007/978-1-4612-0049-9_31.

84. Forsgren, Anders L., and Walter Murray. *Newton Methods for Large-Scale Linear Equality-Constrained Minimization.* Defense Technical Information Center, April 1, 1990. https://doi.org/10.1137/0614040.

85. Bartholomew-Biggs, M. C. “Recursive Quadratic Programming Methods Based on the Augmented Lagrangian.” *Computation Mathematical Programming*, 1987, 21–41. https://doi.org/10.1007/bfb0121177.

86. Zwart, P.B. *Nonlinear Programming: The Global Use of the Lagrange.* Washington Univ., St. Louis, Mo. Dept. of Applied Mathematics and Computer Sciences, United States, October 31, 1970. https://doi.org/10.2172/4138525.

87. Schittkowski, K. “NLPQL: A Fortran Subroutine Solving Constrained Nonlinear Programming Problems.” *Annals of Operations Research* 5, no. 2 (June 1986): 485–500. https://doi.org/10.1007/bf02022087.

88. Schittkowski, Klaus. “NLPQLP: A Fortran Implementation of a Sequential Quadratic Programming Algorithm with Distributed and Non-Monotone Line Search - User's Guide, Version 3.0.” *Softwareentwicklung Schittkowski GmbH*, https://www.schittkowski.de/downloads/numerical/NLPQLP.pdf.

89. Young, C. W., and Budynas, R. G., *Roark’s Formulas for Stress and Strain*, 7th ed., McGraw-Hill, New York, 2002.

90. ANSYS Parametric Design Language Guide, Release 2023 R1, https://ansyshelp.ansys.com/.

91. Bell, John B., et al. “Solutions of Ill-Posed Problems.” *Mathematics of Computation*, vol. 32, no. 144, Oct. 1978, p. 1320. https://doi.org/10.2307/2006360.

92. Dillard, David A. “Fundamentals of Stress Transfer in Bonded Systems.” *Adhesion Science and Engineering*, 2002, 1–44. https://doi.org/10.1016/b978-0-444-51140-9.50028-7.

93. Adams, Robert D., and William C. Wake. *Structural Adhesive Joints in Engineering*, 1984. https://doi.org/10.1007/978-94-009-5616-2.

94. Mitchell, Melanie. *An Introduction to Genetic Algorithms*. The MIT Press, 1998. https://doi.org/10.7551/mitpress/3927.001.000.

95. Wang, Xiyun, and Randy Gu. “Identification of Contact Pressures between Deformable Bodies by Combining Finite Elements and a Novel Hybrid Minimization Strategy.” *Meccanica*, vol. 58, no. 11, Nov. 2023, pp. 2205–18. https://doi.org/10.1007/s11012-023-01722-w.